## Article
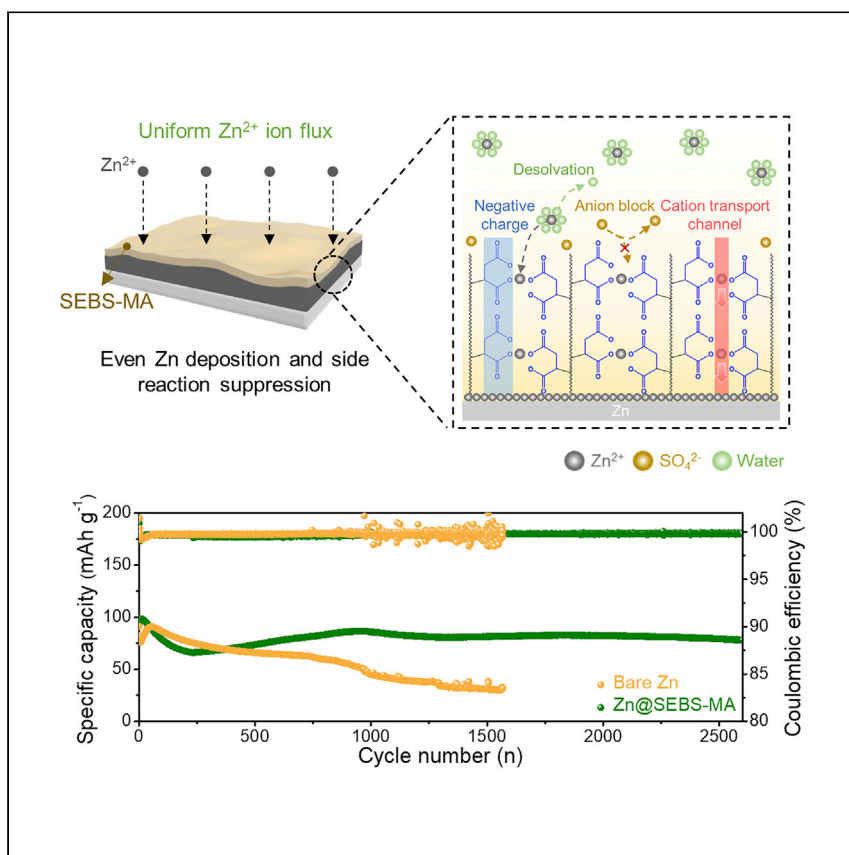
# Ion-selective and chemical-protective elastic block copolymer interphase for durable zinc metal anode



Zn²⁺ Uniform Zn²⁺ ion flux

SEBS-MA

Even Zn deposition and side reaction suppression

Desolvation

Negative charge | Anion block | Cation transport channel

Zn²⁺ | SO₄²⁻ | Water

Sangyeop Lee, Gyujin Song, Sungho Kim, ..., Gahyun Kim, Seok Ju Kang, Soojin Park

soojin.park@postech.ac.kr

### Highlights

Artificial interphase is presented to improve the stability of the zinc anode

SEBS-MA layer induces uniform zinc deposition and prevents side reactions

Characterization methods reveal the ion behavior inside the interphase layer

Lee et al. report a multifunctional polymeric protective layer for zinc anode. The protective layer promotes stable zinc deposition and stabilizes anode interphase with suppressing hydrogen gas evolution and chemical side reactions, leading to a highly durable battery operation.

## Article

# Ion-selective and chemical-protective elastic block copolymer interphase for durable zinc metal anode

Sangyeop Lee,[1] Gyujin Song,[2,4] Sungho Kim,[2] Dong-Yeob Han,[2] Jae Hyun Park,[3] Sungjin Cho,[2] Hye Bin Son,[2] Gahyun Kim,[2] Seok Ju Kang,[3] and Soojin Park[1,2,5,*]

## SUMMARY

Aqueous rechargeable batteries based on zinc anodes are among the most promising systems to replace conventional lithium-ion batteries owing to their intrinsic safety, high ionic conductivity, and economic benefits. However, inferior reversibility of zinc anode resulting from zinc dendrites and surface side reactions limits the practical realization of zinc-ion batteries. Herein, we develop a thin but robust polymeric artificial interphase to enhance reversibility of zinc anode. The grafted maleic anhydride groups in the polymer structure restrain the detrimental reactions through selective zinc-ion penetration and homogenize ion distribution, leading to a smooth electrode surface after plating-stripping processes. Consequently, the coated zinc anode shows excellent stability with a long-term symmetric cell lifespan (>3,000 h at 3 mA·cm$^{-2}$) and maintains capacity retention of 80% after 2,500 cycles, paired with a manganese oxide cathode. This study provides a facile fabrication process and accessible analysis methods to rationalize the development of high-performance zinc-ion batteries.

## INTRODUCTION

The emerging issues of the global energy crisis and climate change have become major problems for our society. Thus, a great deal of research pursuing sustainable energy sources such as wind, solar, and hydropower has explored how to overcome upcoming problems.[1–3] However, sustainable energy sources suffer from uncertainty and instability in power generation since they significantly depend on external environmental factors.[4,5] Consequently, additional energy storage systems (ESSs) are inevitably required to manage excess electricity efficiently and transfer energy timely. Rechargeable batteries that enable the facile conversion and storage of energy produced thus have been extensively investigated as a rational solution for renewable energy sources. In particular, lithium-ion batteries (LIBs) paired with organic solvent-based electrolytes are reported as the most widely used systems presently.[6,7] However, organic solvents have the chance to cause battery explosion by side reactions and chemical degradations inside the batteries.[8,9] Therefore, non-flammable, aqueous-based battery systems have been actively studied as alternatives to conventional LIBs since water media have distinct advantages over organic electrolytes in intrinsic safety, nontoxicity, cost-effectiveness, and outstanding power output.[10,11]

Among various aqueous batteries based on different charge carrier metal cations (Na$^+$, K$^+$, Mg$^{2+}$, Zn$^{2+}$, and Al$^{3+}$),[12–16] aqueous Zn-ion batteries (ZIBs) are studied

[1]Division of Advanced Materials Science, Pohang University of Science and Technology (POSTECH), Pohang 37673, Republic of Korea

[2]Department of Chemistry, Pohang University of Science and Technology (POSTECH), Pohang 37673, Republic of Korea

[3]Department of Energy Engineering, School of Energy and Chemical Engineering, Ulsan National Institute of Science and Technology (UNIST), Ulsan 44919, Republic of Korea

[4]Present address: Secondary Battery Materials Research Laboratory, Research Institute of Industrial Science & Technology (RIST), Pohang 37673, Republic of Korea

[5]Lead contact

*Correspondence: soojin.park@postech.ac.kr

https://doi.org/10.1016/j.xcrp.2022.101070
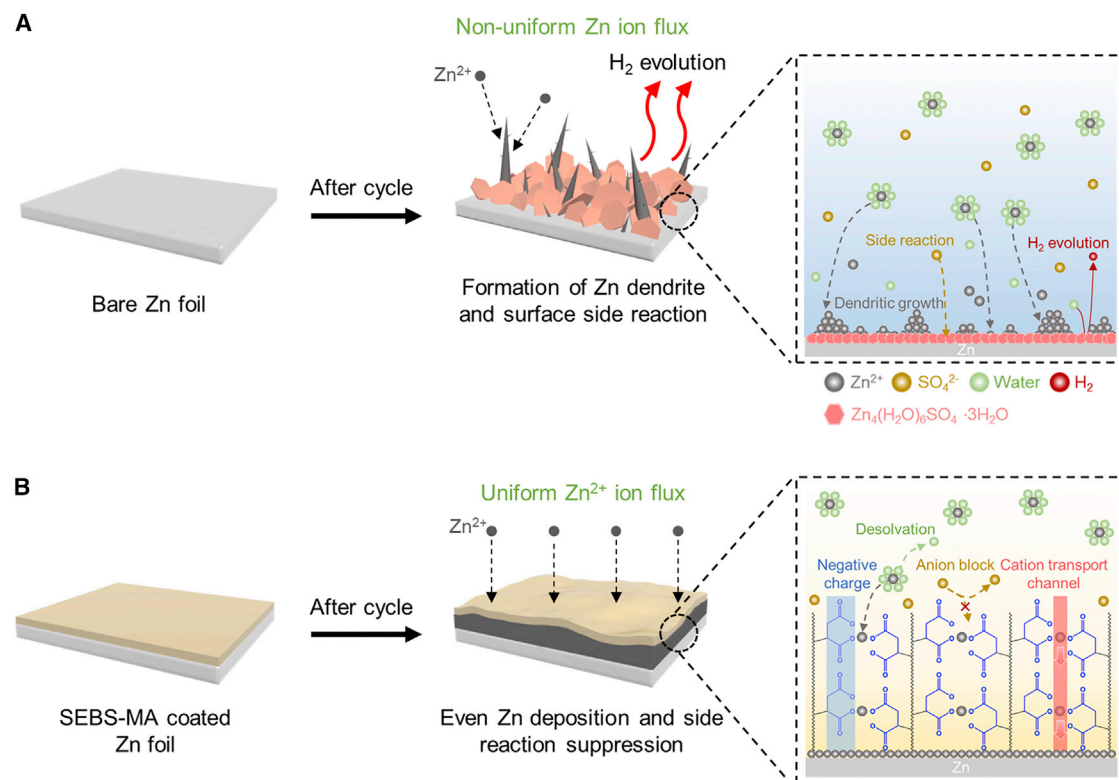
**Figure 1. Schematic illustration of zinc anode during cycling**
(A) Bare zinc foil anode with dendritic growth that involves surface side reactions during cycling.
(B) SEBS-MA coating layer induces smooth electrode surface with uniform $Zn^{2+}$ ion flux and no side reactions.

as the most attractive system owing to the beneficial properties of the Zn anode, including large theoretical capacity (gravimetric capacity of 820 mAh·g$^{-1}$ and volumetric capacity of 5,855 mAh·cm$^{-3}$), low reduction potential (−0.76 V versus standard hydrogen electrode), insensitive manufacturing condition, and low material cost.[17] Despite several existing studies on ZIBs, the practical application of Zn-based ESSs is under challenge due to dendritic growth and low electrochemical reversibility of the Zn anode.[18] Like other metals, Zn tends to form a dendritic architecture during stripping/plating processes due to inhomogeneous charge distribution and surface diffusion, leading to an internal short circuit.[19] Furthermore, Zn dendrite with a large surface area facilitates detrimental surface side reactions to induce insulating by-products (e.g., $Zn_4SO_4(OH)_6 \cdot 5H_2O$), Zn corrosion, and competitive hydrogen evolution reaction (HER) in mild acidic electrolytes (Figure 1A).[20,21] The "detrimental side reactions" incur local environmental change to accelerate dendritic growth and degrade batteries, resulting in low Coulombic efficiency (CE) and subsequent capacity fading.[22] As a result, an effective anode modification strategy is urgently needed to achieve long-cycle life in ZIBs.

Several strategies, such as using a three-dimensional (3D) porous substrate, Zn-metal alloy-based electrode, electrolyte modification, gel polymer electrolytes, and artificial protective layer, reportedly enhance the electrochemical reversibility of the Zn anode and address the remaining challenges.[23–29] Most of all, introducing an artificial protective layer is an attractive method because it can be fabricated by a simple coating process and exhibits tunable electrochemical and mechanical properties according to layer components. Meanwhile, uniform Zn plating and

CellPress
OPEN ACCESS

suppressing the side reaction of electrolytes have been considered vital to improving the working performance of Zn anodes.[30,31] An artificial protective layer can achieve homogeneous $Zn^{2+}$ transfer through the interphase and prevents direct contact between the aqueous electrolyte and the electrode, thereby stabilizing the interface and increasing the lifespan of batteries.[32,33] However, numerous studies on artificial protective layers still require additional improvements because the as-reported interphase layers should be designed with a thick structure to alleviate infinite volume expansion of Zn during the repetitive charge/discharge cycles. Unfortunately, this thick interphase electrochemically brings out negative effect for the overall energy density of batteries. Also, studies on ion behavior inside the protective layer remain in the infant stage, and investigation of ion conduction through the interphase layer is required to develop advanced anode materials.

Herein, polystyrene-*block*-poly(ethylene-*ran*-butylene)-*block*-polystyrene-*graft*-maleic anhydride (SEBS-MA) is introduced as an artificial protective layer for the Zn anode through a simple spin-coating process. The 180-nm-thick SEBS-MA thin film can withstand the volume change of Zn during repetitive charge-discharge processes due to its high stretchability and mechanical robustness (Figure S1). Generally, polar functional groups like carboxylic groups feature anion shielding effect and attract metal cations to align ion migration.[34,35] In the SEBS-MA layer, maleic anhydride functionalities contained in SEBS-MA undergo protonation processes in aqueous condition to form maleic acid, which possesses abundant carboxylic groups. Consequently, they attract $Zn^{2+}$ dissolved in the electrolyte and form a cation transporting channel, leading to a smooth electrode surface without dendritic metal growth as described in Figure 1B. Moreover, this SEBS-MA layer exhibits an ion-selective property, so only $Zn^{2+}$ can pass through the interphase, whereas water molecules and $SO_4^{2-}$ anions are chemically restricted. This ion-selective layer effectively suppresses HER and the formation of detrimental species caused by surface side reactions. Accordingly, the electrochemical reversibility of the Zn anode can be highly improved. Consequently, based on the synergetic effects between the electrode surface stabilization and the uniform ion distribution, the SEBS-MA-coated Zn (denoted as Zn@SEBS-MA) symmetric cell demonstrates ultralong cycle life (>3,200 h) at a high current density of 3 mA·cm$^{-2}$ and an areal capacity of 1 mAh·cm$^{-2}$. The beneficial effect of SEBS-MA was further investigated using Zn@SEBS-MA|MnO$_2$ full cells that exhibit improved rate capability and capacity retention, which maintained 80% of the initial capacity even after 2,500 cycles at 5C.

## RESULTS AND DISCUSSION

### Surface protection of polymer interphase

Polymer layer coated electrodes were prepared using a simple spin-coating process for the SEBS-MA and polystyrene-*block*-poly(ethylene-*ran*-butylene)-*block*-polystyrene (SEBS) polymers. For the SEBS-MA and SEBS copolymers, the Fourier transform infrared spectroscopy (FTIR) results (Figure S2) show that polymer layers were clearly detected on the Zn surface through the existence of newly developed chemical bonds after coating process. The characteristic peaks at 2,920 and 2,850 cm$^{-1}$ represent the C–H stretching in SEBS polymer chains.[36] In contrast, no notable peaks are detected in bare Zn foil, indicating successful surface coating of protective SEBS-MA layers. The polymer-coated Zn foil exhibits peaks at 1,601 cm$^{-1}$, assigned to the C=C stretching of aromatic ring in the polymer structure of SEBS.[37] As expected, compared with the SEBS-coated Zn foil (denoted as Zn@SEBS), the Zn@SEBS-MA demonstrates a characteristic peak at 1,710 cm$^{-1}$ that represents the C=O stretching of maleic anhydride groups grafted on SEBS-MA polymer.[38]
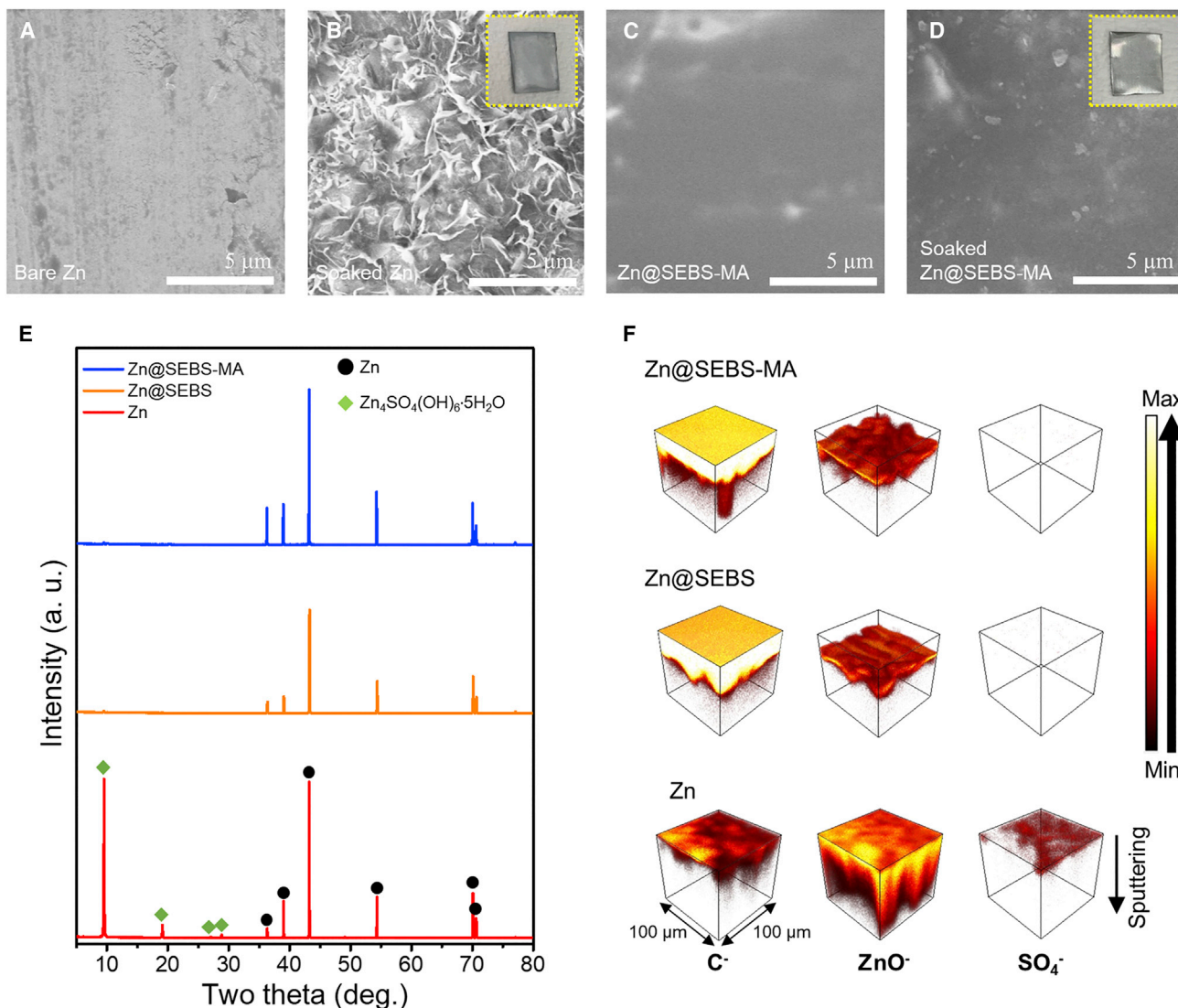
**Figure 2. Suppression of surface degradation by SEBS-MA layer**

(A and B) Top-view SEM images of bare Zn electrode before immersion (A) and after immersion (B) in 2 M ZnSO$_4$ electrolyte for 5 days. Inset in (B) shows photo image of bare Zn after immersion.

(C and D) Top-view SEM images of Zn@SEBS-MA electrode before immersion (C) and after immersion (D) in 2 M ZnSO$_4$ electrolyte for 5 days. Inset in (D) shows photo image of Zn@SEBS-MA after immersion.

(E) XRD patterns of Zn@SEBS-MA, Zn@SEBS, and bare Zn electrode after being soaked in 2 M ZnSO$_4$ electrolyte for 5 days.

(F) Time-of-flight secondary ion mass spectrometry 3D plots of C$^-$, ZnO$^-$, and SO$_4^-$ for three different electrodes.

Qualifications, such as anti-corrosion property and suitable mechanical robustness to entail infinite volume expansion of Zn dendrite during repetitive electrodeposition/dissolution processes, are required to be a rational interphase on the Zn anode. To investigate the surface stabilization of the introduced polymeric layers, Zn electrodes (bare Zn and coated Zn) were immersed in 2 M ZnSO$_4$ electrolyte for 5 days. The morphological change of the surfaces of the electrodes appeared using scanning electron microscopy (SEM). Surface side reactions and Zn corrosion resulted in loosely piled insulating species on the Zn surface that impede a facile charge migration upon the electrode interphase.[39] Accordingly, the surface of bare Zn foil changes from flat to rough structure (Figures 2A and 2B). Unfortunately, the formed by-product layers are highly porous, so they cannot prevent further

## Cell Reports
# Physical Science
Article

**CellPress**
OPEN ACCESS

electrolyte side reactions like the solid electrolyte interphase layer in organic electrolyte-based batteries.[40] Besides the formation of the surface insulating layer, Zn foil lost its intrinsic gloss due to the severe corrosion, which upholds the instability of the Zn foil inside the mild acidic electrolyte system. However, Zn@SEBS-MA and Zn@SEBS maintained smooth surface structure with glossy foil surfaces even after being soaked in an electrolyte, indicating the absence of noticeable surface side reactions or corrosion (Figures 2C, 2D, and S3). The protective effect of SEBS-MA layer was further investigated by obtaining the cross-sectional SEM images, in which cracked flakes, formed by the surface degradation, were only detected on the bare Zn surface after electrolyte immersion (Figure S4).

X-ray diffraction (XRD) patterns were obtained after being soaked in the electrolyte for 5 days (Figure 2E) to further verify the surface by-products' formation. As expected, the XRD patterns of Zn@SEBS-MA and Zn@SEBS exhibit identical XRD peaks corresponding to (002), (100), (101), (102), (103), (110), and (004) planes of a pristine Zn metal (Figure S5). Meanwhile, the XRD pattern of the bare Zn anode after immersion demonstrates the newly formed sharp peaks, indicating the formation of some species (i.e., $Zn_4SO_4(OH)_6 \cdot 5H_2O$) insulating the metal surface due to chemical side reactions of electrolyte.[41] Additionally, after electrolyte immersion, the surface degradation characteristics of the three electrodes (bare Zn, Zn@SEBS-MA, and Zn@SEBS) were quantitatively investigated using time-of-flight secondary ion mass spectrometry (TOF-SIMS) analysis. Figure 2F shows the spatial distribution of $C^-$, $ZnO^-$, and $SO_4^-$ using depth profiling TOF-SIMS plots to confirm the surface stability through artificial interphase. As-prepared Zn@SEBS-MA and Zn@SEBS have intense $C^-$ signals, suggesting the uniform coating layer on the Zn foil surface. However, a small amount of $C^-$ ions are detected around the bare Zn surface, stemming from the natively formed $Zn_5(CO_3)_2(OH)_6$ layer.[42] Due to the blocking effect of the coating layer, intrinsic zinc oxide species with only low intensity appear in the polymer-coated Zn electrodes. In contrast, bare Zn foil shows a continuous distribution of $ZnO^-$ as sputtering proceeds, which supports the surface degradation of Zn after electrolyte contact. Moreover, Zn@SEBS-MA and Zn@SEBS have stable electrode surfaces without noticeable $SO_4^-$ signals, whereas bare Zn exhibits intense $SO_4^-$ signals due to the formation of $Zn_4SO_4(OH)_6 \cdot 5H_2O$, which serves as additional evidence for the electrode protection of the coating layer.

Meanwhile, it has been reported that an elastic and stretchable polymer layer such as SEBS can alleviate the random vertical metal growth.[43] As a result, tensile tests were conducted to investigate the feasibility of the SEBS-MA polymer film as an ultrathin protective layer that can endure volume expansion during battery operation and suppress dendritic growth (Figures S6 and S7). Surprisingly, the mechanical analysis results revealed that the SEBS-MA has sturdy physical properties, high maximum stretchability (>700%), and structural reversibility on repeated deformation cycles under 300% strain showing possibility as a physical barrier.

### Ion-transporting behavior of polymeric layer

The maleic anhydride functional group in SEBS-MA plays a critical role to serve as a protective layer. In essence, the SEBS-MA protective layer is expected to beneficially affect the $Zn^{2+}$ migration through the formation of an ion-transporting channel that results from the electrostatic interaction between maleic anhydride and an aqueous electrolyte (2 M $ZnSO_4$ in deionized water). Hence, to investigate the ion coordination behavior inside the SEBS-MA layer, silicon wafers coated with two different polymers (SEBS and SEBS-MA) were immersed in the electrolyte for 5 days and washed carefully to conduct in-depth molecular distribution in the coating layer
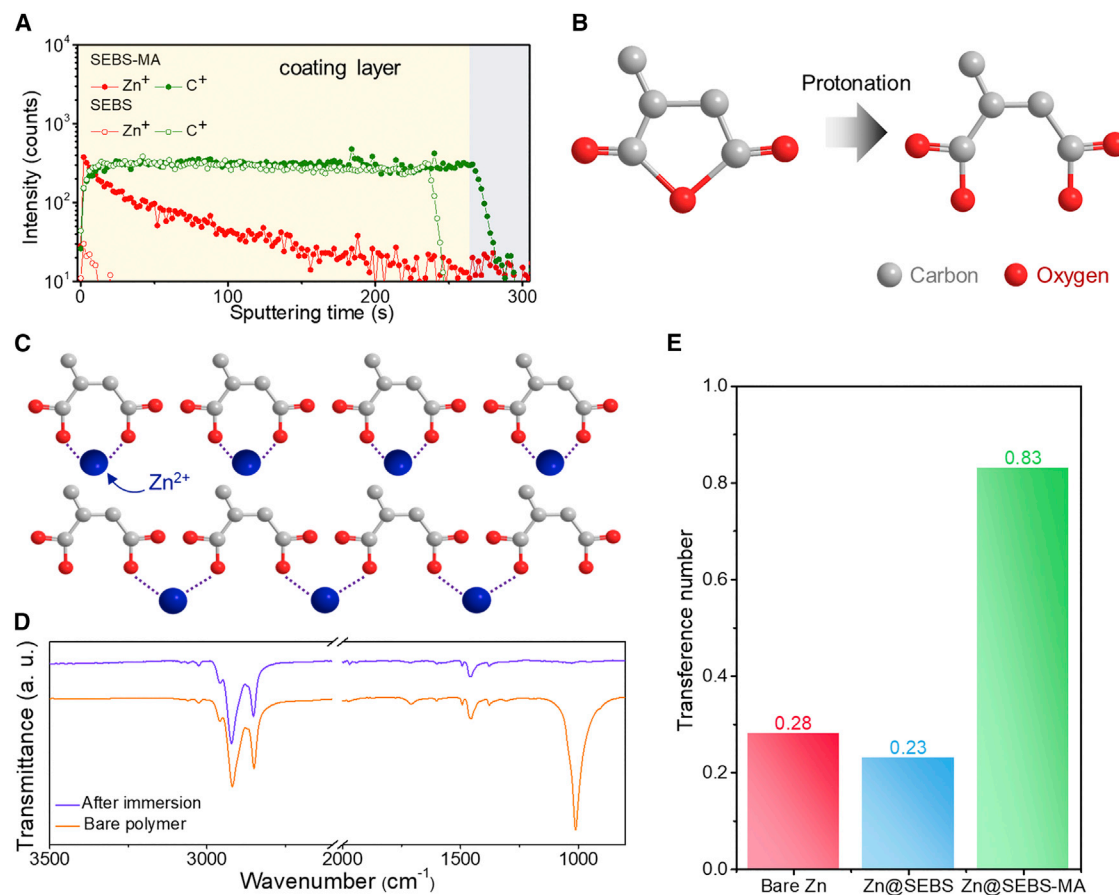
**Figure 3. Illustration of Zn$^{2+}$ transporting effect of the coating layer**

(A) TOF-SIMS plots of Zn$^+$ and C$^+$ for polymer-coated silicon wafers (SEBS-MA and SEBS polymer) after electrolyte immersion in electrolyte for 5 days.

(B) Ring-opening process of maleic anhydride groups. After being soaked in an electrolyte, hydrolysis of maleic anhydride occurs, resulting in CO-$O$-CO bond dissociation.

(C) Schematic illustration of Zn$^{2+}$ coordination behavior.

(D) FTIR spectra of SEBS-MA polymer pellet and Zn@SEBS-MA electrode after immersion in an aqueous electrolyte for 5 days.

(E) Transference number of electrodes (bare Zn, Zn@SEBS, and Zn@SEBS-MA).

through TOF-SIMS analysis. Figure 3A displays the TOF-SIMS results of polymer-coated silicon wafers for Zn$^+$ and C$^+$. Uniform C$^+$ signals are detected in both samples, stemming from the carbon species in the polymer backbone, indicating a uniform coating of both the polymers. However, different distributions of Zn$^+$ appear, such that remarkable amounts of Zn are in the whole SEBS-MA film. In contrast, the SEBS film shows deficient Zn species along the depth, indicating that the SEBS cannot uniformly distribute the Zn-ions due to no realization of ion-coordinating properties in the chemical structure of the sole SEBS copolymer. It is worth noting that the formation of by-products related to surface side reactions are suppressed in the case of the SEBS-MA-coated electrodes, indicating that the detected Zn$^+$ signals originated from the coordinated Zn$^{2+}$ cations inside the polymer layers.

Typically, the maleic anhydride can easily break the ring chain in a polar solvent like water, causing the protonation of the ring structure to produce an acidic form that features the Zn cation-chelating properties in the electrolyte (Figure 3B).[44,45] The suggested ion coordination mechanism of the grafted maleic anhydride, when immersed in an electrolyte, is illustrated in detail (Figure S8). First, as-formed maleic
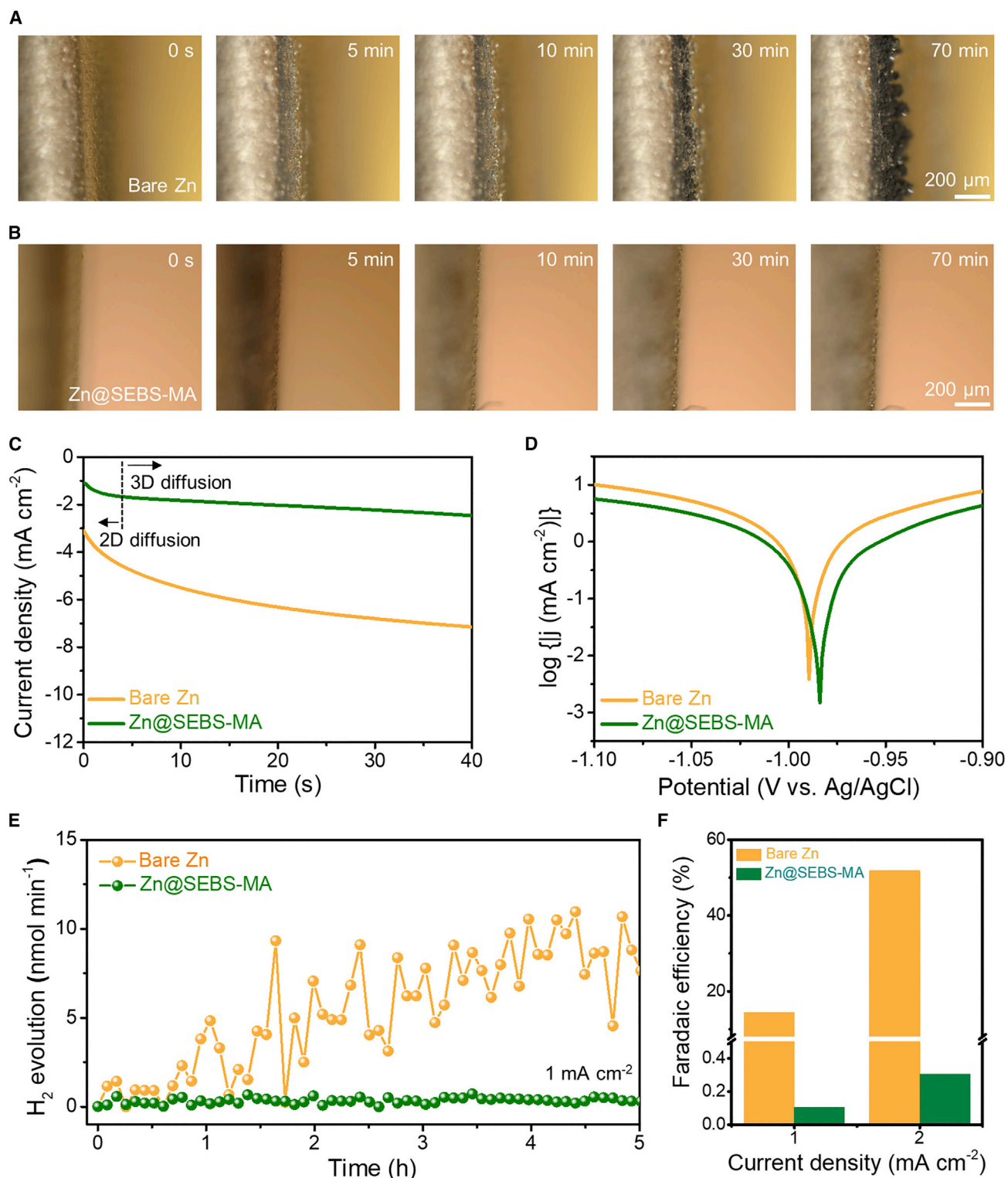
**Figure 4. Uniform Zn deposition during cycling and surface stability against electrochemical reaction in an aqueous electrolyte**

(A and B) *In situ* OM observation of bare Zn (A) and Zn@SEBS-MA (B) under a current density of 10 mA·cm$^{-2}$.

(C) Chronoamperometry results of bare Zn and Zn@SEBS-MA, indicating restrained 3D diffusion of Zn@SEBS-MA.

**Figure 4. Continued**

(D) Linear polarization curves of bare Zn and Zn@SEBS-MA electrodes.

(E) Differential electrochemical mass spectrometry (DEMS) analysis of evolved $H_2$ gas by 1 mA·cm$^{-2}$ constant current application for 5 h.

(F) Faradaic efficiency of bare Zn and Zn@SEBS-MA with different current densities (1 and 2 mA·cm$^{-2}$), showing highly suppressed $H_2$ gas evolution of Zn@SEBS-MA.

acid is hydrated and undergoes two successive proton dissociation processes, which produces the maleate dianion structure that can interact with $Zn^{2+}$ contained in the electrolyte. Accordingly, several negative charges in maleate ions attract the Zn cations and form successive $Zn^{2+}$ coordination groups in polymer structure, which form the Zn-ion-transporting channel in turn. The consequent $Zn^{2+}$ coordination structure is supposed to be a coexistence of two different forms (i.e., two $O^-$ in the one maleate ion interact with the same $Zn^{2+}$, or two $O^-$ in different adjacent maleate ions interact with the same $Zn^{2+}$ cation; Figure 3C).

The ring-opening process of maleic anhydride was further verified by FTIR spectroscopy of a pure SEBS-MA polymer pellet and a free-standing film after electrolyte immersion (Figure 3D). The bare SEBS-MA pellet exhibits the characteristic transmittance peaks of SEBS-MA at 2,920 cm$^{-1}$ (C–H stretching), 2,850 cm$^{-1}$ (C–H stretching), 1,710 cm$^{-1}$ (C=O stretching), and 1,601 cm$^{-1}$ (C=C stretching of aromatic ring), which can be confirmed identically in the Zn@SEBS-MA electrode. Concerning the SEBS-MA pellet, an intense peak at 1,030 cm$^{-1}$ can be attributed to the asymmetric stretching of the C–O–C bond in anhydride groups.[46] The results revealed that maleic anhydride caused the ring-opening to lose the C–O–C chain after electrolyte immersion, enabling the Zn cation coordination and helping to induce ion cloud formation in the whole polymer interphase, like a single-ion conductor to pave the facile ion channels for effective charge transfer. The $Zn^{2+}$ coordination process was further investigated based on X-ray photoelectron spectroscopy (XPS) analysis using SEBS-MA-coated silicon wafer immersed in electrolyte solution for 5 days. As expected, the XPS result shows sharp Zn $2p_{1/2}$ and Zn $2p_{3/2}$ peaks with no obvious S 2p peaks, confirming the coordination behavior of $Zn^{2+}$ toward maleic anhydride functionality (Figure S9). Owing to the formation of an ion-transporting pathway through maleic anhydride, the Zn@SEBS-MA electrode presents a high cation transference number of 0.83, which considerably exceeds those of bare Zn anode and Zn@SEBS (Figures 3E and S10).

### Effect of SEBS-MA layer on electrochemical performance

The ion-conducting behavior of the SEBS-MA layer is expected to induce homogeneous $Zn^{2+}$ distribution and ordered Zn electrodeposition during the long-term cycle life. To estimate the surface homogenizing effect of the SEBS-MA protective layer, *in situ* optical microscopy analysis was conducted by applying a current density of 10 mA·cm$^{-2}$ for the bare Zn and Zn@SEBS-MA electrodes, respectively (see Videos S1 and S2). The mossy architecture of Zn was detected in bare Zn foil only after 5 min of discharge, attributed to the inhomogeneous Zn-ion distribution and subsequent uneven Zn growth (Figure 4A). Furthermore, the formation of Zn dendrites intensifies as current is applied due to the "tip effect," such that the black-colored Zn dendrites cover the whole electrode surface.[47,48] In contrast, the Zn@SEBS-MA presents a smooth electrode surface during the whole electrodeposition process without the formation of noticeable Zn dendrites even under such a high current density (Figure 4B). The electrochemical analysis based on chronoamperometry measurements further demonstrated the stabilizing effect of the SEBS-MA layer on the electrode (Figure 4C). In the current as a function of time under the constant potential polarization of −150 mV, the initial stage of the discharge process represents the initial Zn nucleation and two-dimensional (2D) diffusion of $Zn^0$ species

and the following region indicates the degree of 3D diffusion affected by the early stages.[49,50] As expected from the *in situ* observation results, the bare Zn anode suffers from the prevalent surface diffusion as the 3D diffusion current increases steadily, indicating a large volume expansion and porous structure establishment on the Zn electrodeposition. In contrast, the Zn@SEBS-MA could sufficiently restrain the 3D diffusion on prolonged electrodeposition, reflecting the lateral spread of Zn-ion distribution during Zn deposition, leading to a formation of dense Zn inside the powerful polymer interphase.

In addition to the electrodeposition behavior, the electrochemical stability of the Zn anode in an aqueous electrolyte is another important factor intimately associated with the operating properties.[51,52] Unlike the bare Zn anode, the Zn@SEBS-MA anode is likely resistant to aqueous medium-induced side reactions including metal corrosion, formation of passivation layers, and HER attributed to the $Zn^{2+}$ selective pathways. The anti-corrosion effect of the SEBS-MA was estimated using linear polarization curves under 2 M $ZnSO_4$ electrolyte conditions for both the bare Zn and Zn@SEBS-MA electrodes (Figure 4D). Generally, the corrosion potential and current are indicators of corrosion behavior, so higher corrosion potential indicates more resistance to electrode corrosion, whereas lower corrosion current implies tardy corrosion.[53] The Tafel polarization curves in Figure S11 present the corrosion-protective effect of the SEBS-MA layer with corrosion potential of −0.9839 V (versus Ag/AgCl) and corrosion current of 2.123 mA·$cm^{-2}$, which are much improved values compared with bare Zn anode. As well as the electrode corrosion, HER has been regarded as one of the critical issues that detrimentally influences battery operation. To evaluate the HER quantitatively, differential electrochemical mass spectrometry (DEMS) analysis in terms of hydrogen gas was conducted under a constant current of 1 mA·$cm^{-2}$ for 5 h (Figure 4E). Apparently, both the bare Zn and Zn@SEBS-MA anodes showed suppressed gas generation until an hour. However, at a prolonged discharge state, the amount of the produced $H_2$ gas in the unit time steadily increased on bare Zn anode, supposedly resulting from the rough electrode surface. In contrast, the Zn@SEBS-MA continuously suppressed the formation of $H_2$ gas for 5 h (5 mAh·$cm^{-2}$); there was a similar tendency in the DEMS analysis at an elevated current density of 2 mA $cm^{-2}$ (see Figure S12). Consequently, the Zn@SEBS-MA shows extremely low Faradaic efficiency values of $H_2$ evolution of 0.105% and 0.305% for current densities of 1 and 2 mA·$cm^{-2}$, respectively, whereas values of 14.45% and 51.86% were calculated for the bare Zn electrode, respectively (Figure 4F). The impressive results indicate that the SEBS-MA interphase effectively manipulates the unexpected chemical reaction, including surface corrosion and HER effect, as well as enhanced electrochemical behavior when used in aqueous Zn-based batteries.

### Electrochemical characterization of Zn@SEBS-MA anode

Notably, the interphase thickness was carefully optimized. Thickness values outside the optimized range cause untimely cell failure, which can be attributable to the poor physical endurance and insufficient ion-transporting behavior (Figures S13 and S14). Accordingly, all experiments conducted herein were based on the Zn@SEBS-MA electrode with a thickness of 180 nm and the Zn@SEBS electrode with a similar coating layer thickness. Owing to the ion-transporting channel and side reaction suppression of the SEBS-MA layer, the Zn@SEBS-MA electrode is expected to present superior cycling performance. Thus, the electrochemical behaviors of the bare Zn, Zn@SEBS, and Zn@SEBS-MA electrodes were investigated under a symmetrical coin-type cell system using a 2 M $ZnSO_4$ electrolyte. First, three electrodes were operated at an areal capacity of 1 mAh·$cm^{-2}$ under a current density of 1 mA·$cm^{-2}$
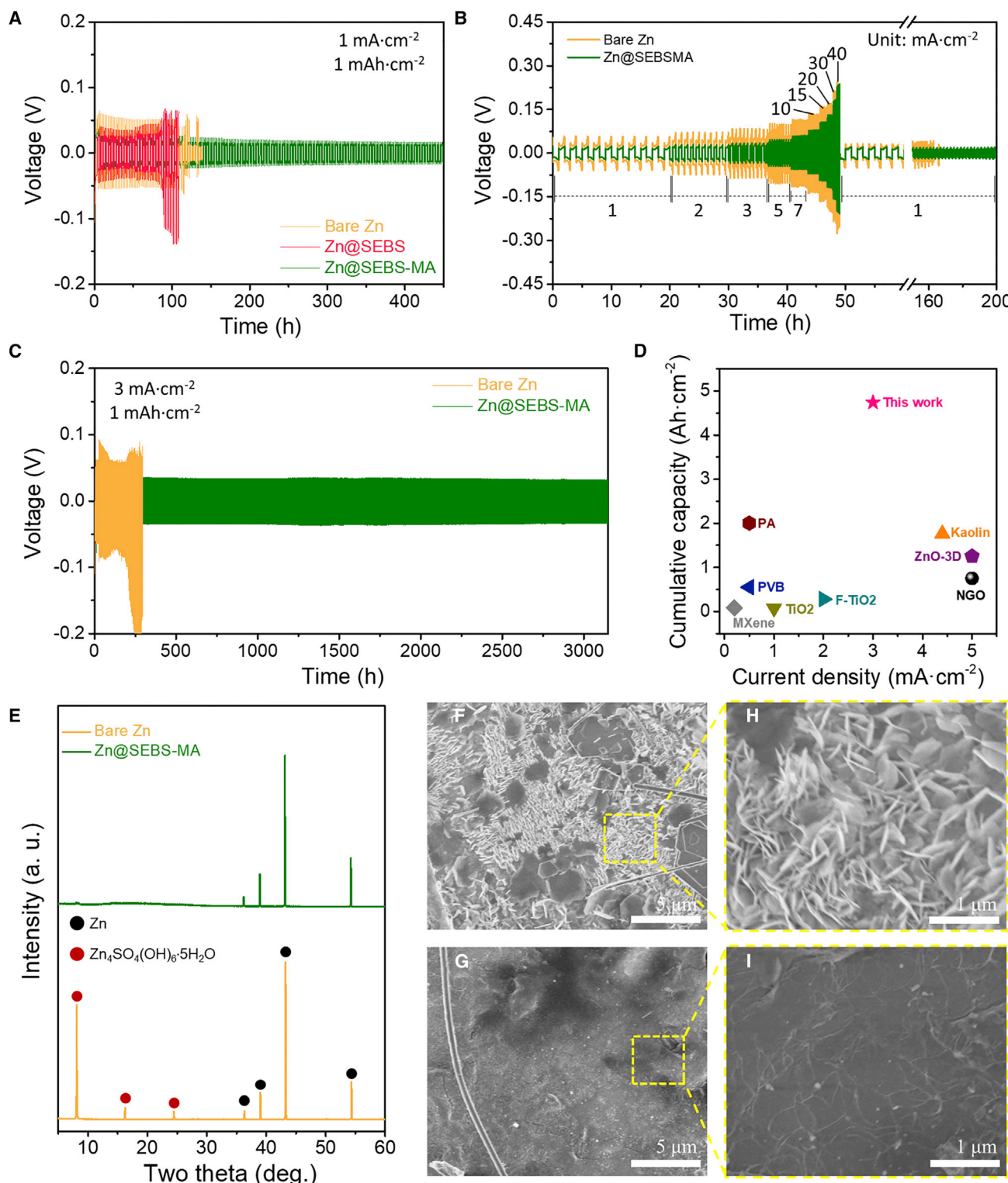
**Figure 5. Zn plating/stripping behavior characteristics of different symmetrical cells**

(A) Cycling performance of symmetric cells based on bare Zn, Zn@SEBS, and Zn@SEBS-MA anodes at 1 mA·cm$^{-2}$ current density.

(B) Rate performance of bare Zn and Zn@SEBS-MA symmetric cells at various current densities (for current density of 1, 2, 3, 5, 7, 10, 15, 20, 30, and 40 mA·cm$^{-2}$). After 40 mA·cm$^{-2}$, the current density was recovered to 1 mA·cm$^{-2}$. Areal capacity is 1 mAh·cm$^{-2}$.

(C) Long-term galvanostatic cycling of bare Zn, Zn@SEBS, and Zn@SEBS-MA symmetric cells at 3 mA·cm$^{-2}$ current density.

**Figure 5. Continued**

(D) Cumulative capacity and current density comparison of Zn@SEBS-MA electrode with as-reported studies.

(E) XRD patterns of bare Zn and Zn@SEBS-MA electrodes after 15 plating-stripping cycles, where black and red dots indicate Zn and $Zn_4SO_4(OH)_6 \cdot 5H_2O$ respectively.

(F and G) Top-view SEM images of bare Zn (F) and Zn@SEBS-MA (G) anode after 15 cycles.

(H and I) Enlarged top-view SEM images at dashed squares of bare Zn (H) and Zn@SEBS-MA (I).

(Figure 5A). All three electrodes reveal stable cycling behavior in the early cycles with almost identical plating/stripping voltage profiles. In comparison, as the working time passes, the cells based on bare Zn and Zn@SEBS suffer from a large overpotential with irregular voltage profiles, resulting from surface side reactions and limited ion-transporting effect of SEBS interphase. In contrast, the Zn@SEBS-MA-based cell exhibits stable electrochemical behaviors for 400 h owing to the beneficial properties of the SEBS-MA interphase. Furthermore, a rate capability test was conducted with increasing current density from 1 to 40 mA·cm$^{-2}$ to estimate the beneficial properties of SEBS-MA artificial layer toward facile charge transfer. As shown in Figure 5B, the Zn@SEBS-MA exhibited more stable cycling behavior even up to 40 mA·cm$^{-2}$ and successfully recovered its initial voltage profiles when tuning the current density to 1 mA·cm$^{-2}$. Based on the critical current density investigation, the long-term cyclability of the symmetrical cells were further tested at an areal capacity of 1 mAh·cm$^{-2}$ and a high current density of 3 mA·cm$^{-2}$ (Figure 5C). The voltage hysteresis is the voltage difference between plating and stripping, mostly affected by the surface properties and charge transfer resistance.[54,55] Severe voltage fluctuations are observed in the voltage-time graph of the bare Zn anode with large voltage hysteresis along the overall cycle time. On the other hand, the Zn@SEBS-MA-based cell shows an extremely durable cycle life of >3,200 h and low voltage hysteresis (<80 mV). The efficient interphase developed herein toward long-term cycle stability showed remarkable achievement compared with other recently reported Zn anodes (Figure 5D and Table S1).[40,56–62]

In order to investigate the excellent working behavior of the SEBS-MA coated electrode, a postmortem analysis of bare Zn and Zn@SEBS-MA anodes was conducted after operating the symmetric cells. The XRD results in Figure 5E reveal that inescapable amounts of insulating species (i.e., $Zn_4SO_4(OH)_6 \cdot 5H_2O$) were formed on the surface of the bare Zn anode due to severe side reactions at the interface between the aqueous electrolyte and the Zn anode. However, the Zn@SEBS-MA anode remained intact without evident insulating species, which is attributable to the $Zn^{2+}$-selective property of the SEBS-MA layer that directly blocks the direct contact between the aqueous media and the electrode surface while transporting $Zn^{2+}$ ions. The durability of Zn@SEBS-MA was further examined using SEM after cycling. As shown in the top-view SEM image of Figures 5F and 5H, the bare Zn anode showed a highly impaired electrode surface, so sharp and vertically grown Zn species are clear on the overall surface. Such a rough surface negatively affects the cycling behavior since it facilitates side reactions and can induce internal short circuit across the separator, which in turn causes cell failure. On the contrary, the Zn@SEBS-MA electrode presents a smooth electrode surface without unexpected by-produced-derived roughness in both the low- and high-magnification images, supporting the ion distribution effect of the SEBS-MA layer that results in the uniform Zn plating/stripping behavior during cycling (Figures 5G and 5I).

Moreover, full cells were assembled to investigate the practical application of the Zn@SEBS-MA electrode by pairing it with a carbon nanotube (CNT)-modified birnessite manganese dioxide cathode (denoted as $MnO_2$). The synthesized $MnO_2$ was

identified using XRD analysis, and the product showed a porous flower-like structure along with CNT fibers (Figure S15). The full cells were estimated using 2 M $ZnSO_4$ + 0.2 M $MnSO_4$ electrolyte, where 0.2 M $MnSO_4$ salt was added to compensate for the dissolution of $Mn^+$ species in the $MnO_2$ cathode.[63] The cyclic voltammetry curves of the two cells ($Zn|MnO_2$ and $Zn@SEBS-MA|MnO_2$) show almost identical electrochemical behavior corresponding to typical redox pairs of birnessite-based ZIBs, as reported in previous studies (Figure 6A).[64,65] Furthermore, both cells exhibit similar voltage profiles under galvanostatic charge/discharge processes with clear $H^+$ and $Zn^{2+}$ insertion regions, while the Zn@SEBS-MA-based cell presents a slightly higher charge capacity associated with the modified anode interphase (Figure S16). The anode stabilization effect on the rate performance was investigated under varying current densities from 0.5C to 20C (1C = 99.1 mA·cm$^{-2}$) as depicted in Figure 6B. In the first five cycles at 0.5C, both cells cycle stably, such that almost unchanged capacities are obtained. Interestingly, the Zn@SEBS-MA cell exhibits stable capacity variations, while bare $Zn|MnO_2$ presents fast capacity drop, accompanying the capacity fluctuation due to the deteriorated anode.

Further, the long-term cycle performances of full cells were evaluated (Figure 6C). The Zn@SEBS-MA cell suffers from capacity decay in the early stages induced by the intrinsic $MnO_2$ phase transformation.[66] However, after the phase transformation, the cell shows a gradual capacity recovery and stable cycling behavior at 5C, thereby enabling the capacity retention of 80% even after 2,500 cycles. Also, the Zn@SEBS-MA-based cell exhibits a superior CE of 99.7% after the phase deformation steps, indicating its feasibility for practical purposes. The long-term durability of Zn@SEBS-MA is ascribed to a beneficial effect of the SEBS-MA layer that induces a dendrite-free electrode surface and suppresses detrimental side reactions. The bare Zn anode-based cell suffers from analogous capacity fade, while it undergoes continuous capacity decay since the formation of Zn dendrites and severe side reactions accelerate the damage in electrochemical behaviors. The remarkable electrochemical property of Zn@SEBS-MA can be further rationalized by comparing voltage profiles of the second and 1,000[th] cycles (Figures 6D and 6E). In both cells, bare Zn and Zn@SEBS-MA exhibited similar electrochemical behaviors in the second cycle, respectively. In the 1,000[th] cycle of the Zn@SEBS-MA cell, an intact voltage profile appears without considerable capacity degradation; thus, more than 90% of the charge capacity can be maintained. However, the bare Zn anode reveals a contrasting trend, such that only about a half of the charge capacity is retained after 1,000 cycles, indicating incompatibility in long-term operation. Hence, these results support that the SEBS-MA is a promising protective layer species that enables long-term cyclability through side reaction suppression and ion-regulating functionalities.

In summary, we constructed a thin and powerful SEBS-MA interphase to effectively restrain both the chemical and electrochemical degradation before and during battery cycling. The ring-opening process of the MA group formed the facile $Zn^{2+}$ pathway and blocked the direct contact of water and reactive anion with the Zn electrode, leading to anti-corrosion properties related to hydrogen evolution and surface destruction. Furthermore, the SEBS copolymer as the main backbone flexibly controlled the Zn morphology from unexpected dendrite growth. Thus, the artificial interphase finally enabled lateral and dense Zn electrodeposition up to 10 mA·cm$^{-2}$, unveiled through *in situ* optical microscopy observation. Furthermore, the stable Zn deposition-dissolution processes during long-term cycle life without metal depletion or chemical decomposition of the electrolyte resulted in a cumulative capacity of 4,740 mAh·cm$^{-2}$ under a current density of 3 mA·cm$^{-2}$. Based on these enhancements, we realized fast-charging and stable full cells paired with

**Cell Reports**
**Physical Science**
Article

CellPress
OPEN ACCESS
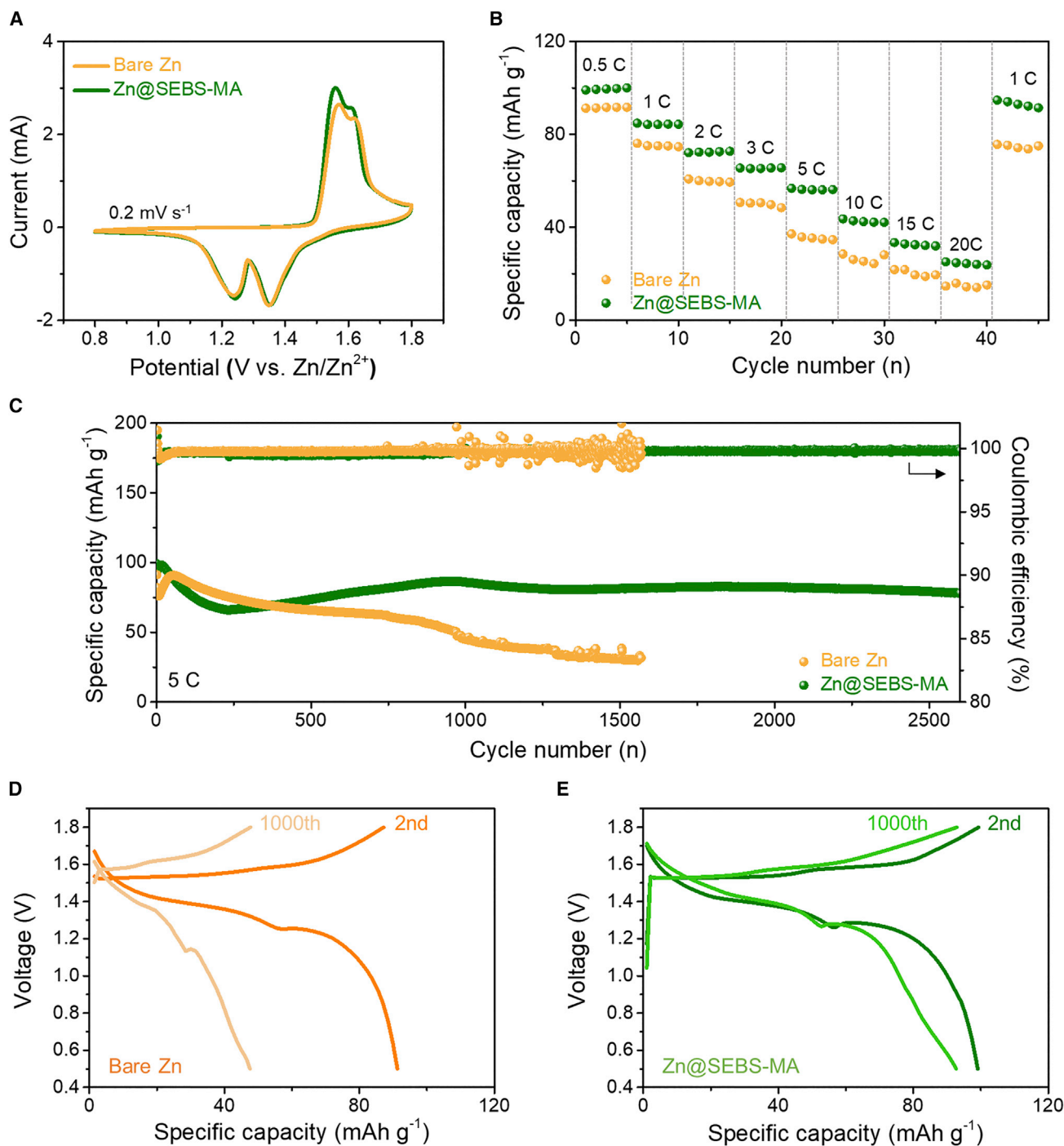


**Figure 6. Full cell electrochemical characterization**

(A) Cyclic voltammetry curves of Zn|MnO$_2$ and Zn@SEBS-MA|MnO$_2$ cells at 0.2 mV s$^{-1}$ scan rate.

(B) Rate performance comparison of Zn and Zn@SEBS-MA electrodes.

(C) Long-term cycling performance and corresponding Coulombic efficiency at 5C cycle rate of Zn|MnO$_2$ and Zn@SEBS-MA|MnO$_2$ cells.

(D and E) Charge/discharge profiles at second and 1,000$^{th}$ cycles of Zn|MnO$_2$ (D) and Zn@SEBS-MA|MnO$_2$ (E) cells.

MnO$_2$ cathode over 2,500 cycles at 5C without fatal electrochemical degradation with the help of a thin SBES-MA layer on Zn. This study provides an effective design strategy with an ultrathin and versatile polymer structure as the artificial interphase

**CellPress**
OPEN ACCESS

**Cell Reports**
**Physical Science**
Article

and is further expected to open a large-scale system market of Zn-based aqueous rechargeable batteries with the application of a practical system using comma coater and roll-to-roll equipment.

## EXPERIMENTAL PROCEDURES

### Resource availability

#### Lead contact
Further information and requests for resources should be directed to and will be fulfilled by the lead contact, Soojin Park (soojin.park@postech.ac.kr).

#### Materials availability
This study did not generate new materials.

#### Data and code availability
All data generated during the study are available from the lead contact upon reasonable request. This study did not generate a code.

### Preparation of Zn@SEBS-MA electrodes
The Zn@SEBS-MA electrodes were fabricated using the facile spin-coating method. Here, different concentrations (1, 3, and 5 wt %) of SEBS-MA (Sigma-Aldrich) polymer pellets were dissolved in toluene under vigorous stirring. The Zn foils were washed with ethanol before spin-coating. Subsequently, the polymer solutions were spin-coated at 1,000 rpm for 60 s on Zn foils (125 μm). Then, the Zn@SEBS-MA electrodes were obtained after drying in an inert argon condition.

### Synthesis of $MnO_2$-CNT cathode material
Modified $MnO_2$ was prepared according to a previous study.[67] First, 100 mg of commercially available multiwalled CNTs (Hanhwa Solutions) and 2.5 g of $KMnO_4$ (Sigma-Aldrich) were ground homogeneously using an agate mortar. After grinding, the mixed powder was transferred to a glass vial and dispersed in 100 mL of deionized water with vigorous stirring for 10 min. Next, 0.5 mL of concentrated $H_2SO_4$ (Junsei Chemical) was added to the mixture with stirring for 30 min, which was transferred to the oil bath and heated at 80°C for 1 h with constant stirring. Afterward, the mixture was cooled to room temperature naturally, and the reactant was collected using vacuum filtration and washed with deionized water repeatedly. Finally, the resulting precipitate was dried at 60°C overnight to obtain $MnO_2$@CNT.

### Cell assembly
The Zn|$MnO_2$ full cells were prepared as follows: $MnO_2$@CNT, carbon black, and polyvinylidene fluoride (PVDF) were mixed uniformly at a weight ratio of 7:1:2 and dispersed in N-methyl-2-pyrrolidone (NMP) to prepare the cathode slurry. Then, the prepared slurry was coated on carbon paper (WizMAC) and vacuum dried at 80°C for 15 h. The dried carbon paper was pressed using a roll press machine and punched into disks (Φ = 12 mm). Meanwhile, bare Zn and the Zn@SEBS-MA foils were punched into disks (Φ = 14 mm) and used as the anode. The coin cells were assembled by pairing the zinc anode with an as-prepared cathode using glass fiber and 2 M $ZnSO_4$ + 0.2 M $MnSO_4$ aqueous solution as the separator and electrolyte respectively. The mass loading of cathode active materials (total mass of CNT and $MnO_2$) was ~2–3 mg·cm$^{-2}$. Zn–Zn symmetric cells were prepared using two identical bare Zn and the Zn@SEBS-MA electrodes, punched into disks, and assembled in 2032-type coin cells. An aqueous electrolyte of 2 M $ZnSO_4$ (Sigma-Aldrich) was employed as a mild acidic electrolyte, coupled with a glass fiber separator. All

electrochemical measurements were tested at 25°C using sufficient 2 M $ZnSO_4$ electrolyte, except for the cathode-paired full cells.

## Material characterization

To investigate the side reaction suppression, XRD patterns of the Zn electrodes were obtained by powder XRD (Rigaku Smartlab) with Cu Kα radiation ($\lambda$ = 1.5406 Å). Field-emission scanning electron microscopy (FE-SEM, Hitachi S-4800) was used to collect images of the surfaces of the Zn electrode and the $MnO_2$@CNT morphology. The ion coordination effect of the SEBS-MA coating layer in the aqueous electrolyte was investigated using FTIR (Agilent Technologies Cary 600) at a resolution of 4 $cm^{-1}$. The mechanical properties of the polymer layer were investigated using a universal tensile machine (Petrol LAB DA-01) at a constant strain rate of 5 $mm \cdot min^{-1}$. Time-of-flight secondary ion mass spectrometry (TOF-SIMS) 3D profiling and depth analysis was conducted with IonTOF TOF-SIMS 5. A stylus profilometer (Bruker DektakXT) was employed to measure the coated polymer layer thickness.

## Electrochemical measurements

Galvanostatic charge/discharge measurements were conducted using a battery cycler system (Wonatech WBCS3000Le). The galvanostatic characterization on symmetric cells was performed after the initial electrode stabilization cycle at 0.5 $mA \cdot cm^{-2}$. Cyclic voltammetry (CV) and electrochemical impedance spectroscopy (EIS) were measured by an electrochemical workstation (Bio-logic Science Instruments VMP-300). In detail, the CV of Zn|$MnO_2$ cells was conducted under a scan rate of 0.2 $mV \cdot s^{-1}$ at a potential range of 0.8–1.8 V. To measure the transference number, the EIS spectra of the symmetric cells were investigated under the potentiostatic EIS mode condition with 10 mV amplitude and a frequency range of 1 MHz–10 mHz. Furthermore, to identify the diffusion behavior during the initial Zn plating, chronoamperometry was performed in a three-electrode configuration. Bare Zn or the SEBS-MA-coated Zn, bare Zn foil, and Ag/AgCl (saturated KCl) served as the working, counter, and reference electrodes, respectively. The applied potential polarization was 150 mV. The corrosion behavioral characteristics of zinc anodes were characterized using a linear polarization curve with a three-electrode configuration. Bare Zn or the SEBS-MA-coated Zn, bare Zn foil, and Ag/AgCl (saturated KCl) served as the working, counter, and reference electrodes, respectively. The corrosion current and corrosion potential were calculated from Tafel fit analysis in the electrochemical workstation. The electrode morphology change during plating was investigated using *in situ* optical microscopy (Olympus BX53M) at a current density of 10 $mA \cdot cm^{-2}$. Bare Zn or Zn@SEBS-MA served as the working electrode and bare Zn foil for reference and counter electrodes. The transference number of $Zn^{2+}$ ($t_{Zn^{2+}}$) was investigated using a symmetric cell system based on the EIS results before and after the chronoamperometry tests and calculated by the following equation:

$$t_{Zn^{2+}} = \frac{I_s(\Delta V - I_0 R_0)}{I_0(\Delta V - I_s R_s)}, \qquad \text{(Equation 1)}$$

where $\Delta V$ is the applied potential polarization, $I_0$ and $R_0$ are the current and resistance of the initial state, respectively, and $I_s$ and $R_s$ are the steady-state current and resistance, respectively. The applied potential polarization is 10 mV. Hydrogen gas evolution was evaluated using *in situ* DEMS under continuous argon gas flow. The evolved gaseous species were collected every 5 min. The Faradaic efficiency of $H_2$ evolution was evaluated under the DEMS system by the following equation:

**CellPress**
OPEN ACCESS

**Cell Reports**
**Physical Science**
Article

$$\text{Faradaic efficiency (\%)} = \frac{N_{H_2} \times F \times n}{Q} \times 100, \qquad \text{(Equation 2)}$$

where Q, F, and $N_{H_2}$ represent the total quantity of charge passed, Faraday constant (96,485 C mol$^{-1}$), and the total amount of hydrogen produced, respectively. Here n = 2 for a two-electron reaction. Measurement was conducted using a hole-perforated 2032-type coin cell.

## SUPPLEMENTAL INFORMATION

## ACKNOWLEDGMENTS

## AUTHOR CONTRIBUTIONS

Conceptualization, S.L. and G.S.; formal analysis, S.L., G.S., D.-Y.H., J.H.P., S.J.K., and S.C.; investigation, S.L., S.K., G.K., and H.B.S.; methodology, G.S., S.K., and S.P.; resources, S.L. and S.K.; writing – original draft, S.L., G.S., and S.P.; funding acquisition, S.P.; supervision, S.P.

## DECLARATION OF INTERESTS

The authors declare no competing interests.

## REFERENCES

1. Luderer, G., Madeddu, S., Merfort, L., Ueckerdt, F., Pehl, M., Pietzcker, R., Rottoli, M., Schreyer, F., Bauer, N., Baumstark, L., et al. (2022). Impact of declining renewable energy costs on electrification in low-emission scenarios. Nat. Energy 7, 32–42. https://doi.org/10.1038/s41560-021-00937-z.

2. Cherp, A., Vinichenko, V., Tosun, J., Gordon, J.A., and Jewell, J. (2021). National growth dynamics of wind and solar power compared to the growth required for global climate targets. Nat. Energy 6, 742–754. https://doi.org/10.1038/s41560-021-00863-0.

3. Tong, D., Farnham, D.J., Duan, L., Zhang, Q., Lewis, N.S., Caldeira, K., and Davis, S.J. (2021). Geophysical constraints on the reliability of solar and wind power worldwide. Nat. Commun. 12, 6146. https://doi.org/10.1038/s41467-021-26355-z.

4. Yang, Y., Bremner, S., Menictas, C., and Kay, M. (2018). Battery energy storage system size determination in renewable energy systems: a review. Renew. Sustain. Energy Rev. 91, 109–125. https://doi.org/10.1016/j.rser.2018.03.047.

5. Wu, Y., Zhang, T., Gao, R., and Wu, C. (2021). Portfolio planning of renewable energy with energy storage technologies for different applications from electricity grid. Appl. Energy 287, 116562. https://doi.org/10.1016/j.apenergy.2021.116562.

6. Merryweather, A.J., Schnedermann, C., Jacquet, Q., Grey, C.P., and Rao, A. (2021). Operando optical tracking of single-particle ion dynamics in batteries. Nature 594, 522–528. https://doi.org/10.1038/s41586-021-03584-2.

7. Qiao, L., Oteo, U., Martinez-Ibañez, M., Santiago, A., Cid, R., Sanchez-Diez, E., Lobato, E., Meabe, L., Armand, M., and Zhang, H. (2022). Stable non-corrosive sulfonimide salt for 4-V-class lithium metal batteries. Nat. Mater. 21, 455–462. https://doi.org/10.1038/s41563-021-01190-1.

8. Liu, K., Liu, Y., Lin, D., Pei, A., and Cui, Y. (2018). Materials for lithium-ion battery safety. Sci. Adv. 4, eaas9820. https://doi.org/10.1126/sciadv.aas9820.

9. Larsson, F., Andersson, P., Blomqvist, P., and Mellander, B.E. (2017). Toxic fluoride gas emissions from lithium-ion battery fires. Sci. Rep. 7, 10018. https://doi.org/10.1038/s41598-017-09784-z.

10. Xiao, P., Li, H., Fu, J., Zeng, C., Zhao, Y., Zhai, T., and Li, H. (2022). An anticorrosive zinc metal anode with ultra-long cycle life over one year. Energy Environ. Sci. 15, 1638–1646. https://doi.org/10.1039/D1EE03882F.

11. Chao, D., Zhou, W., Xie, F., Ye, C., Li, H., Jaroniec, M., and Qiao, S.Z. (2020). Roadmap for advanced aqueous batteries: from design of materials to applications. Sci. Adv. 6, eaba4098. https://doi.org/10.1126/sciadv.aba4098.

12. Meng, P., Huang, J., Yang, Z., Wang, F., Lv, T., Zhang, J., Fu, C., and Xiao, W. (2022). A low-cost and air-stable rechargeable aluminum-ion battery. Adv. Mater. 34, 2106511. https://doi.org/10.1002/adma.202106511.

13. Zhou, M., Bai, P., Ji, X., Yang, J., Wang, C., and Xu, Y. (2021). Electrolytes and interphases in potassium ion batteries. Adv. Mater. 33, 2003741. https://doi.org/10.1002/adma.202003741.

14. Bae, J., Park, H., Guo, X., Zhang, X., Warner, J.H., and Yu, G. (2021). High-performance magnesium metal batteries: via switching the passivation film into a solid electrolyte interphase. Energy Environ. Sci. 14, 4391–4399. https://doi.org/10.1039/D1EE00614B.

15. Zhang, H., Gao, Y., Liu, X., Yang, Z., He, X., Li, L., Qiao, Y., Chen, W., Zeng, R., Wang, Y., and Chou, S. (2022). Organic cathode materials for sodium-ion batteries: from fundamental research to potential commercial application. Adv. Funct. Mater. 32, 2107718. https://doi.org/10.1002/adfm.202107718.

16. Zhao, Z., Wang, R., Peng, C., Chen, W., Wu, T., Hu, B., Weng, W., Yao, Y., Zeng, J., Chen, Z., et al. (2021). Horizontally arranged zinc platelet electrodeposits modulated by fluorinated covalent organic framework film for high-rate and durable aqueous zinc ion batteries. Nat. Commun. 12, 6606. https://doi.org/10.1038/s41467-021-26947-9.

17. Wang, N., Wan, H., Duan, J., Wang, X., Tao, L., Zhang, J., and Wang, H. (2021). A review of zinc-based battery from alkaline to acid. Mater. Today Adv. 11, 100149. https://doi.org/10.1016/j.mtadv.2021.100149.

18. Wu, J., Yuan, C., Li, T., Yuan, Z., Zhang, H., and Li, X. (2021). Dendrite-free zinc-based battery with high areal capacity via the region-induced deposition effect of turing membrane. J. Am. Chem. Soc. 143, 13135–13144. https://doi.org/10.1021/jacs.1c04317.

19. Zheng, J., Zhao, Q., Tang, T., Yin, J., Quilty, C.D., Renderos, G.D., Liu, X., Deng, Y., Wang, L., Bock, D.C., et al. (2019). Reversible epitaxial electrodeposition of metals in battery anodes. Science 366, 645–648. https://doi.org/10.1126/science.aax6873.

20. Zhang, T., Tang, Y., Guo, S., Cao, X., Pan, A., Fang, G., Zhou, J., and Liang, S. (2020). Fundamentals and perspectives in developing zinc-ion battery electrolytes: a comprehensive review. Energy Environ. Sci. 13, 4625–4665. https://doi.org/10.1039/D0EE02620D.

21. Yang, J., Cao, J., Peng, Y., Yang, W., Barg, S., Liu, Z., Kinloch, I.A., Bissett, M.A., and Dryfe, R.A.W. (2020). Unravelling the mechanism of rechargeable aqueous Zn–MnO2 batteries: implementation of charging process by electrodeposition of MnO2. ChemSusChem 13, 4103–4110. https://doi.org/10.1002/cssc.202001216.

22. Hoang Huy, V.P., Hieu, L.T., and Hur, J. (2021). Zn metal anodes for Zn-ion batteries in mild aqueous electrolytes: challenges and strategies. Nanomaterials 11, 2746. https://doi.org/10.3390/nano11102746.

23. Guo, W., Cong, Z., Guo, Z., Chang, C., Liang, X., Liu, Y., Hu, W., and Pu, X. (2020). Dendrite-free Zn anode with dual channel 3D porous frameworks for rechargeable Zn batteries. Energy Storage Mater. 30, 104–112. https://doi.org/10.1016/j.ensm.2020.04.038.

24. Wang, S.B., Ran, Q., Yao, R.Q., Shi, H., Wen, Z., Zhao, M., Lang, X.Y., and Jiang, Q. (2020). Lamella-nanostructured eutectic zinc–aluminum alloys as reversible and dendrite-free anodes for aqueous rechargeable batteries. Nat. Commun. 11, 1634. https://doi.org/10.1038/s41467-020-15478-4.

25. Qiu, H., Du, X., Zhao, J., Wang, Y., Ju, J., Chen, Z., Hu, Z., Yan, D., Zhou, X., and Cui, G. (2019). Zinc anode-compatible in-situ solid electrolyte interphase via cation solvation modulation. Nat. Commun. 10, 5374. https://doi.org/10.1038/s41467-019-13436-3.

26. Wu, C., Xie, K., Ren, K., Yang, S., and Wang, Q. (2020). Dendrite-free Zn anodes enabled by functional nitrogen-doped carbon protective layers for aqueous zinc-ion batteries. Dalton Trans. 49, 17629–17634. https://doi.org/10.1039/D0DT03459B.

27. Zhang, B., Qin, L., Fang, Y., Chai, Y., Xie, X., Lu, B., Liang, S., and Zhou, J. (2022). Tuning Zn2+ coordination tunnel by hierarchical gel electrolyte for dendrite-free zinc anode. Sci. Bull. 67, 955–962. https://doi.org/10.1016/j.scib.2022.01.027.

28. Ruan, P., Liang, S., Lu, B., Fan, H.J., and Zhou, J. (2022). Design strategies for high-energy-density aqueous zinc batteries. Angew. Chem. Int. Ed. Engl. 61, e202200598. https://doi.org/10.1002/anie.202200598.

29. Liu, Z., Qin, L., Lu, B., Wu, X., Liang, S., and Zhou, J. (2022). Issues and opportunities facing aqueous Mn2+/MnO2-based batteries. ChemSusChem 15, e202200348. https://doi.org/10.1002/cssc.202200348.

30. Kang, L., Cui, M., Jiang, F., Gao, Y., Luo, H., Liu, J., Liang, W., and Zhi, C. (2018). Nanoporous CaCO3 coatings enabled uniform Zn stripping/plating for long-life zinc rechargeable aqueous batteries. Adv. Energy Mater. 8, 1801090. https://doi.org/10.1002/aenm.201801090.

31. Hong, L., Wu, X., Ma, C., Huang, W., Zhou, Y., Wang, K.X., and Chen, J.S. (2021). Boosting the Zn-ion transfer kinetics to stabilize the Zn metal interface for high-performance rechargeable Zn-ion batteries. J. Mater. Chem. 9, 16814–16823. https://doi.org/10.1039/D1TA03967A.

32. Yang, Y., Liu, C., Lv, Z., Yang, H., Cheng, X., Zhang, S., Ye, M., Zhang, Y., Chen, L., Zhao, J., and Li, C.C. (2021). Redistributing Zn-ion flux by interlayer ion channels in Mg-Al layered double hydroxide-based artificial solid electrolyte interface for ultra-stable and dendrite-free Zn metal anodes. Energy Storage Mater. 41, 230–239. https://doi.org/10.1016/j.ensm.2021.06.002.

33. Chen, P., Yuan, X., Xia, Y., Zhang, Y., Fu, L., Liu, L., Yu, N., Huang, Q., Wang, B., Hu, X., et al. (2021). An artificial polyacrylonitrile coating layer confining zinc dendrite growth for highly reversible aqueous zinc-based batteries. Adv. Sci. 8, 2100309. https://doi.org/10.1002/advs.202100309.

34. Zhang, W., Zhuang, H.L., Fan, L., Gao, L., and Lu, Y. (2018). A "cation-anion regulation" synergistic anode host for dendrite-free lithium metal batteries. Sci. Adv. 4, eaar4410. https://doi.org/10.1126/sciadv.aar4410.

35. Li, M., Li, Z., Wang, X., Meng, J., Liu, X., Wu, B., Han, C., and Mai, L. (2021). Comprehensive understanding of the roles of water molecules in aqueous Zn-ion batteries: from electrolytes to electrode materials. Energy Environ. Sci. 14, 3796–3839. https://doi.org/10.1039/D1EE00030F.

36. Park, H.S., and Hong, C.K. (2021). Anion exchange membrane based on sulfonated poly (Styrene-ethylene-butylene-styrene) copolymers. Polymers 13, 1669. https://doi.org/10.3390/polym13101669.

37. Aguilar-Bolados, H., Quijada, R., Yazdani-Pedram, M., Maldonado-Magnere, S., Verdejo, R., and Lopez-Manchado, M.A. (2020). SEBS-

grafted itaconic acid as compatibilizer for elastomer nanocomposites based on BaTiO3 particles. Polymers 12, 643. https://doi.org/10.3390/polym12030643.

38. Sangeetha, V.H., Varghese, T.O., and Nayak, S.K. (2016). Toughening of polylactic acid using styrene ethylene butylene styrene: mechanical, thermal, and morphological studies. Polym. Eng. Sci. 56, 669–675. https://doi.org/10.1002/pen.24293.

39. Jiao, Y., Li, F., Jin, X., Lei, Q., Li, L., Wang, L., Ye, T., He, E., Wang, J., Chen, H., et al. (2021). Engineering polymer glue towards 90% zinc utilization for 1000 hours to make high-performance Zn-ion batteries. Adv. Funct. Mater. 31, 2107652. https://doi.org/10.1002/adfm.202107652.

40. Hao, J., Li, X., Zhang, S., Yang, F., Zeng, X., Zhang, S., Bo, G., Wang, C., and Guo, Z. (2020). Designing dendrite-free zinc anodes for advanced aqueous zinc batteries. Adv. Funct. Mater. 30, 2001263. https://doi.org/10.1002/adfm.202001263.

41. Chu, Y., Zhang, S., Wu, S., Hu, Z., Cui, G., and Luo, J. (2021). In situ built interphase with high interface energy and fast kinetics for high performance Zn metal anodes. Energy Environ. Sci. 14, 3609–3620. https://doi.org/10.1039/D1EE00308A.

42. Zhang, Z., Said, S., Smith, K., Zhang, Y.S., He, G., Jervis, R., Shearing, P.R., Miller, T.S., and Brett, D.J.L. (2021). Dendrite suppression by anode polishing in zinc-ion batteries. J. Mater. Chem. 9, 15355–15362. https://doi.org/10.1039/D1TA02682H.

43. Song, G., Hwang, C., Song, W.J., Lee, J.H., Lee, S., Han, D.Y., Kim, J., Park, H., Song, H.K., and Park, S. (2022). Breathable artificial interphase for dendrite-free and chemo-resistive lithium metal anode. Small 18, 2105724. https://doi.org/10.1002/smll.202105724.

44. Yang, B., and An, Q. (2021). Density functional theory-assisted synthesis of self-curing epoxy–acrylic resin. Front. Chem. 8, 595954. https://doi.org/10.3389/fchem.2020.595954.

45. Nara, M., Morii, H., and Tanokura, M. (2013). Coordination to divalent cations by calcium-binding proteins studied by FTIR spectroscopy. Biochim. Biophys. Acta 1828, 2319–2327. https://doi.org/10.1016/j.bbamem.2012.11.025.

46. Lin, S.Y., Cheng, W.T., Wei, Y.S., and Lin, H.L. (2011). DSC-FTIR microspectroscopy used to investigate the heat-induced intramolecular cyclic anhydride formation between Eudragit e and PVA copolymer. Polym. J. 43, 577–580. https://doi.org/10.1038/pj.2011.15.

47. Hou, Z., Gao, Y., Tan, H., and Zhang, B. (2021). Realizing high-power and high-capacity zinc/sodium metal anodes through interfacial chemistry regulation. Nat. Commun. 12, 3083. https://doi.org/10.1038/s41467-021-23352-0.

48. Tian, H., Li, Z., Feng, G., Yang, Z., Fox, D., Wang, M., Zhou, H., Zhai, L., Kushima, A., Du, Y., et al. (2021). Stable, high-performance, dendrite-free, seawater-based aqueous batteries. Nat. Commun. 12, 237. https://doi.org/10.1038/s41467-020-20334-6.

49. Xie, S., Li, Y., Li, X., Zhou, Y., Dang, Z., Rong, J., and Dong, L. (2022). Stable zinc anodes

**CellPress**
OPEN ACCESS

**Cell Reports**
**Physical Science**
Article

enabled by zincophilic Cu nanowire networks. Nano Micro Lett. 14, 39. https://doi.org/10.1007/s40820-021-00783-4.

50. Zhou, M., Guo, S., Li, J., Luo, X., Liu, Z., Zhang, T., Cao, X., Long, M., Lu, B., Pan, A., et al. (2021). Surface-preferred crystal plane for a stable and reversible zinc anode. Adv. Mater. 33, 2100187. https://doi.org/10.1002/adma.202100187.

51. Shi, J., Sun, T., Bao, J., Zheng, S., Du, H., Li, L., Yuan, X., Ma, T., and Tao, Z. (2021). Water-in-Deep eutectic solvent" electrolytes for high-performance aqueous Zn-ion batteries. Adv. Funct. Mater. 31, 2102035. https://doi.org/10.1002/adfm.202102035.

52. Zhang, Y., Wu, Y., You, W., Tian, M., Huang, P.W., Zhang, Y., Sun, Z., Ma, Y., Hao, T., and Liu, N. (2020). Deeply rechargeable and hydrogen-evolution-suppressing zinc anode in alkaline aqueous electrolyte. Nano Lett. 20, 4700–4707. https://doi.org/10.1021/acs.nanolett.0c01776.

53. Wang, J., Huang, Y., Liu, B., Li, Z., Zhang, J., Yang, G., Hiralal, P., Jin, S., and Zhou, H. (2021). Flexible and anti-freezing zinc-ion batteries using a guar-gum/sodium-alginate/ethylene-glycol hydrogel electrolyte. Energy Storage Mater. 41, 599–605. https://doi.org/10.1016/j.ensm.2021.06.034.

54. Yang, C.P., Yin, Y.X., Zhang, S.F., Li, N.W., and Guo, Y.G. (2015). Accommodating lithium into 3D current collectors with a submicron skeleton towards long-life lithium metal anodes. Nat. Commun. 6, 8058. https://doi.org/10.1038/ncomms9058.

55. Qi, L., Shang, L., Chen, X., Ye, L., Zhang, W., Feng, P., Zou, W., Cao, N., Zhou, H., Weitz, D.A., and Li, X. (2018). A versatile strategy to fabricate 3D conductive frameworks for lithium metal anodes. Adv. Mater. Interfaces 5, 1800807. https://doi.org/10.1002/admi.201800807.

56. Zhang, N., Huang, S., Yuan, Z., Zhu, J., Zhao, Z., and Niu, Z. (2021). Direct self-assembly of MXene on Zn anodes for dendrite-free aqueous zinc-ion batteries. Angew. Chem. Int. Ed. Engl. 60, 2861–2865. https://doi.org/10.1002/anie.202012322.

57. Zhou, J., Xie, M., Wu, F., Mei, Y., Hao, Y., Huang, R., Wei, G., Liu, A., Li, L., and Chen, R. (2021). Ultrathin surface coating of nitrogen-doped graphene enables stable zinc anodes for aqueous zinc-ion batteries. Adv. Mater. 33, 2101649. https://doi.org/10.1002/adma.202101649.

58. Deng, C., Xie, X., Han, J., Tang, Y., Gao, J., Liu, C., Shi, X., Zhou, J., and Liang, S. (2020). A sieve-functional and uniform-porous Kaolin layer toward stable zinc metal anode. Adv. Funct. Mater. 30, 2000599. https://doi.org/10.1002/adfm.202000599.

59. Zhao, Z., Zhao, J., Hu, Z., Li, J., Li, J., Zhang, Y., Wang, C., and Cui, G. (2019). Long-life and deeply rechargeable aqueous Zn anodes enabled by a multifunctional brightener-inspired interphase. Energy Environ. Sci. 12, 1938–1949. https://doi.org/10.1039/C9EE00596J.

60. Zhao, K., Wang, C., Yu, Y., Yan, M., Wei, Q., He, P., Dong, Y., Zhang, Z., Wang, X., and Mai, L. (2018). Ultrathin surface coating enables stabilized zinc metal anode. Adv. Mater. Interfaces 5, 1800848. https://doi.org/10.1002/admi.201800848.

61. Zhang, Q., Luan, J., Huang, X., Wang, Q., Sun, D., Tang, Y., Ji, X., and Wang, H. (2020). Revealing the role of crystal orientation of protective layers for stable zinc anode. Nat. Commun. 11, 3961. https://doi.org/10.1038/s41467-020-17752-x.

62. Xie, X., Liang, S., Gao, J., Guo, S., Guo, J., Wang, C., Xu, G., Wu, X., Chen, G., and Zhou, J. (2020). Manipulating the ion-transfer kinetics and interface stability for high-performance zinc metal anodes. Energy Environ. Sci. 13, 503–510. https://doi.org/10.1039/C9EE03545A.

63. Sun, W., Wang, F., Hou, S., Yang, C., Fan, X., Ma, Z., Gao, T., Han, F., Hu, R., Zhu, M., and Wang, C. (2017). Zn/MnO$_2$ battery chemistry with H$^+$ and Zn$^{2+}$ coinsertion. J. Am. Chem. Soc. 139, 9775–9778. https://doi.org/10.1021/jacs.7b04471.

64. Zhai, X.Z., Qu, J., Hao, S.M., Jing, Y.Q., Chang, W., Wang, J., Li, W., Abdelkrim, Y., Yuan, H., and Yu, Z.Z. (2020). Layered birnessite cathode with a displacement/intercalation mechanism for high-performance aqueous zinc-ion batteries. Nano Micro Lett. 12, 56. https://doi.org/10.1007/s40820-020-0397-3.

65. Li, G., Huang, Z., Chen, J., Yao, F., Liu, J., Li, O.L., Sun, S., and Shi, Z. (2020). Rechargeable Zn-ion batteries with high power and energy densities: a two-electron reaction pathway in birnessite MnO$_2$ cathode materials. J. Mater. Chem. 8, 1975. https://doi.org/10.1039/C9TA11985J.

66. Wang, L., and Zheng, J. (2020). Recent advances in cathode materials of rechargeable aqueous zinc-ion batteries. Mater. Today Adv. 7, 100078. https://doi.org/10.1016/j.mtadv.2020.100078.

67. Xia, H., Wang, Y., Lin, J., and Lu, L. (2012). Hydrothermal synthesis of MnO$_2$/CNT nanocomposite with a CNT core/porous MnO$_2$ sheath hierarchy architecture for supercapacitors. Nanoscale Res. Lett. 7, 33. https://doi.org/10.1186/1556-276X-7-33.

## Supplemental information

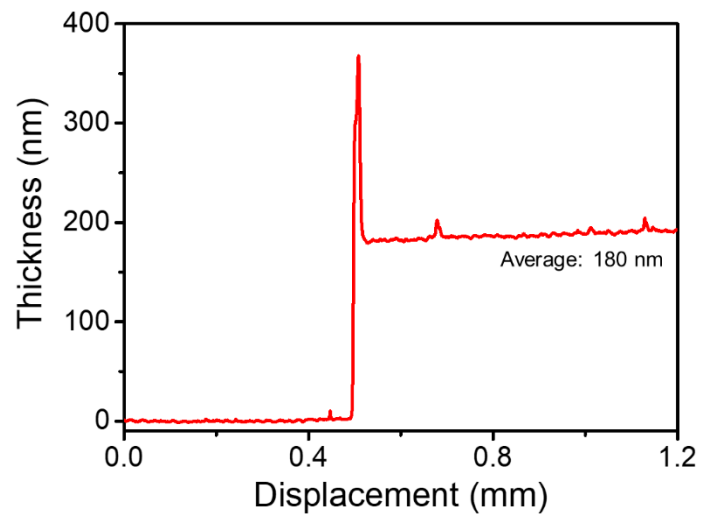# Ion-selective and chemical-protective

# elastic block copolymer

# interphase for durable zinc metal anode

Sangyeop Lee, Gyujin Song, Sungho Kim, Dong-Yeob Han, Jae Hyun Park, Sungjin Cho, Hye Bin Son, Gahyun Kim, Seok Ju Kang, and Soojin Park

**Supplemental Information**

**Figure S1**. SEBS-MA coated zinc electrode thickness profile. Average thickness of the SEBS-MA layer was obtained as 180 nm.
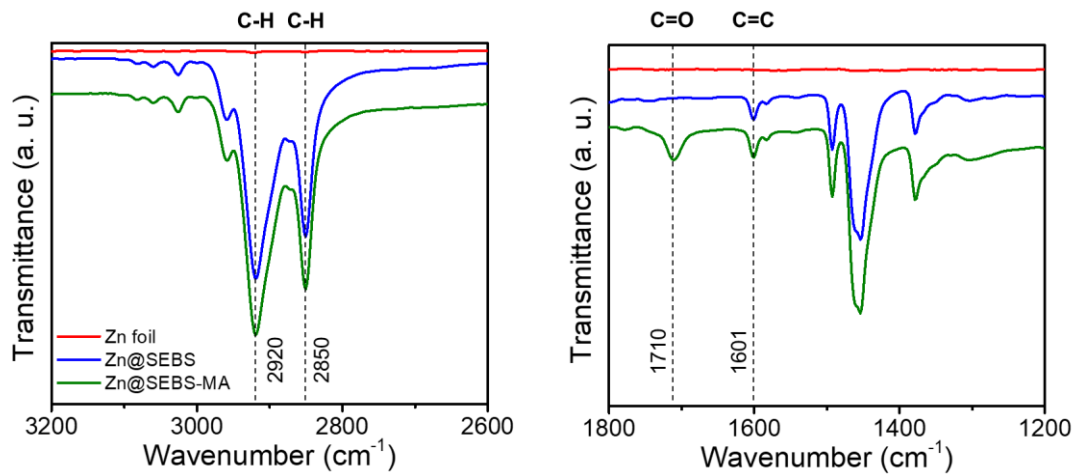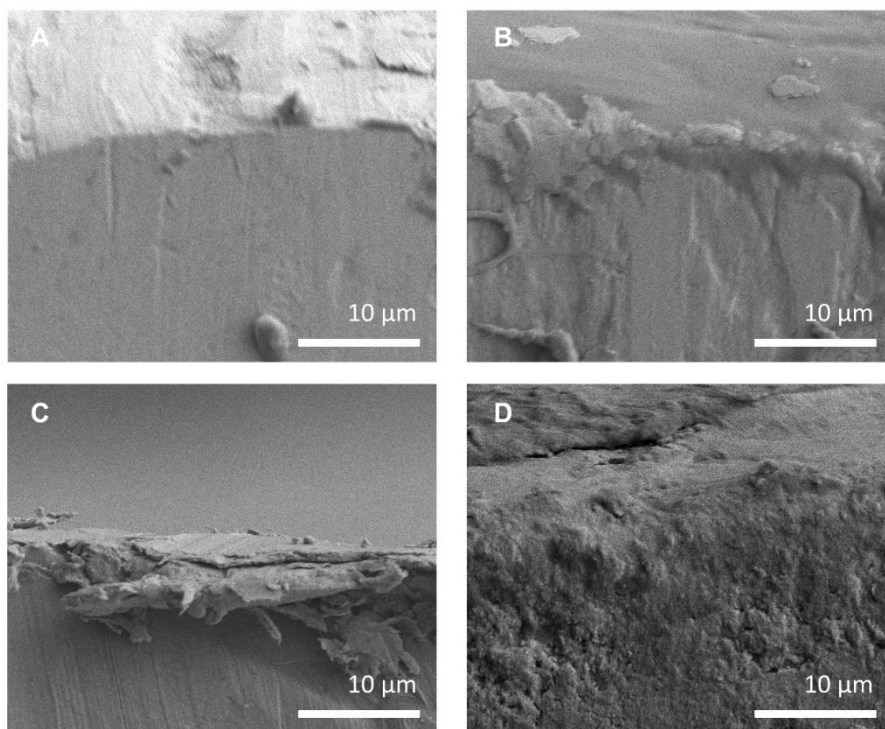
**Figure S2**. FTIR spectra of bare Zn and polymer coated Zn foils. Transmittance peaks at 2920 $cm^{-1}$ and 2850 $cm^{-1}$ represent C-H stretching, while peaks at 1710 $cm^{-1}$ and 1601 $cm^{-1}$ indicate C=O stretching and carbon-carbon stretching of aromatic ring in styrene respectively.
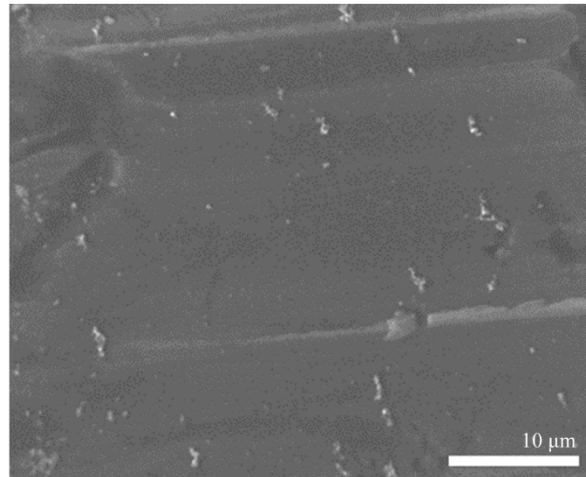
**Figure S3.** Top-view SEM image of Zn@SEBS-MA electrode after immersion in 2 M $ZnSO_4$ electrolyte.

**Figure S4.** Cross-sectional SEM images of electrodes before and after electrolyte soaking. Cross-sectional SEM images of (A) bare Zn foil (A) and (B) Zn@SEBS-MA before electrolyte immersion. Cross-sectional SEM images of (C) bare Zn foil and (D) Zn@SEBS-MA after electrolyte immersion.
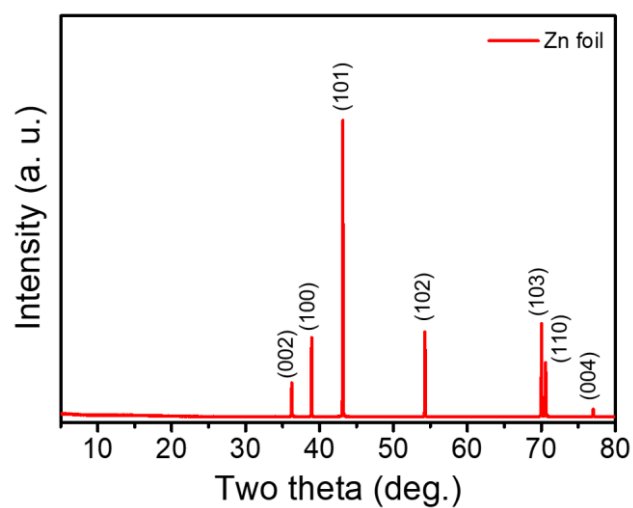
**Figure S5.** XRD pattern of the pristine Zn foil where sharp peaks at 36.2°, 38.9°, 43.2°, 54.3°, 70.0°, 70.6° and 77.0° present (002), (100), (101), (102), (103), (110) and (004) planes of Zn respectively.[1]
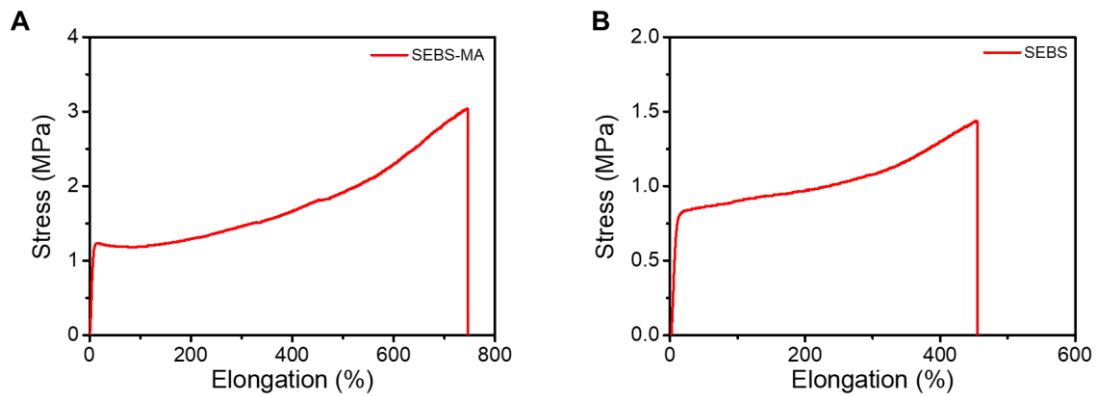
**Figure S6.** Tensile test results of the polymer films.

A mechanical analysis of (A) the SEBS-MA film and (B) SEBS film estimated under the constant strain rate of 5 mm·s$^{-1}$.
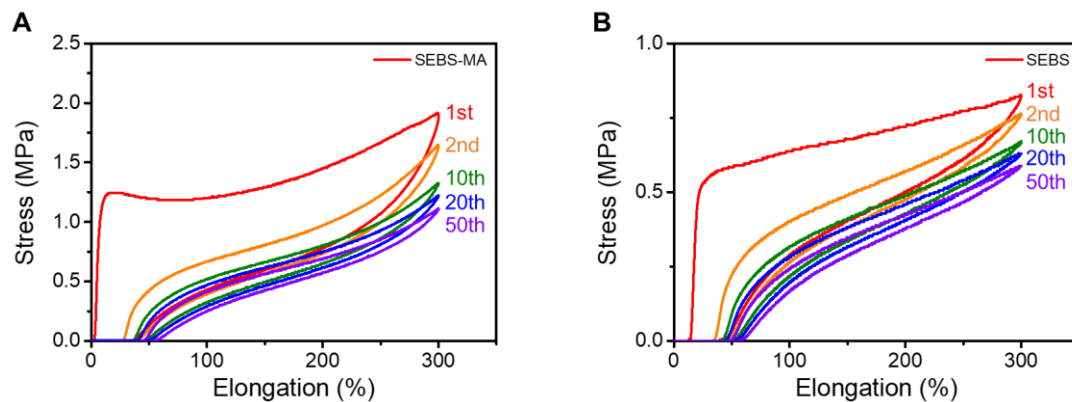
**Figure S7.** Repetitive tensile test results of the polymer films.

Cyclic elongation results of (A) the SEBS-MA film and (B) SEBS film estimated under the constant strain rate of 5 mm·s$^{-1}$ for 300% stretch.

**Step 1**: Protonation of the maleic anhydride groups

Protonation

SEBS-MA polymer

Maleic acid grafted SEBS
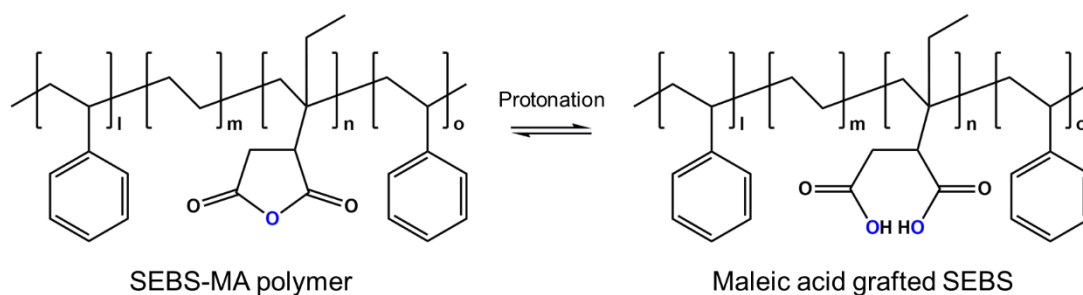
**Step 2**: Proton dissociation processes

Sequential dissociation

Maleate dianion form
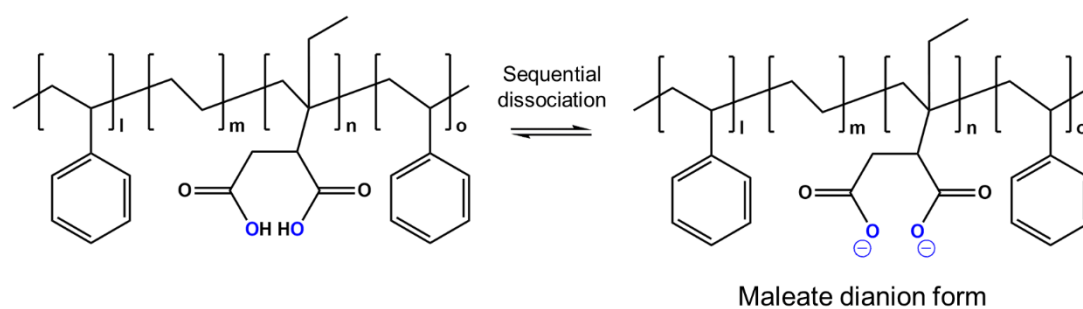
**Step 3**: Zn²⁺ coordination process

Zn²⁺
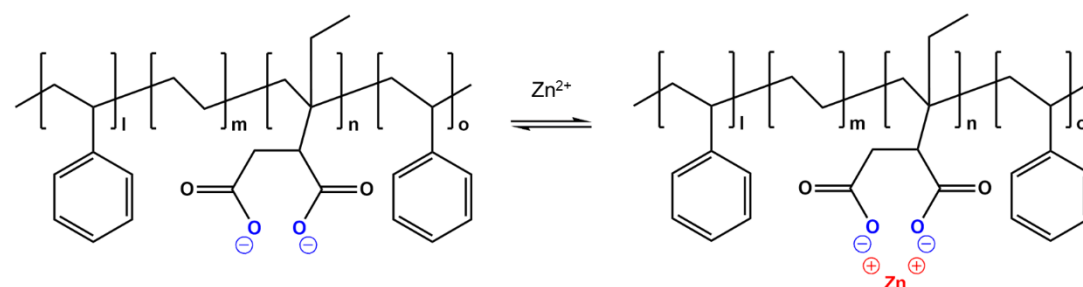
**Figure S8.** Suggested ion coordination mechanism of maleic anhydride groups in SEBS-MA layer in 2 M ZnSO₄ aqueous electrolyte. First, maleic anhydride groups undergo protonation step resulting in the dissociation of CO-O-CO bond (O=C-O-C=O + 2H⁺ → 2O=C-OH). At the same time, maleic anhydride groups turn into acidic form. Next, two consecutive proton dissociation processes occur which induce partial negative charges under aqueous system (2COOH → 2COO⁻ + 2H⁺). Finally, the negative charge of the proton-dissociated acid groups attracts Zn²⁺ cations contained in the electrolyte.
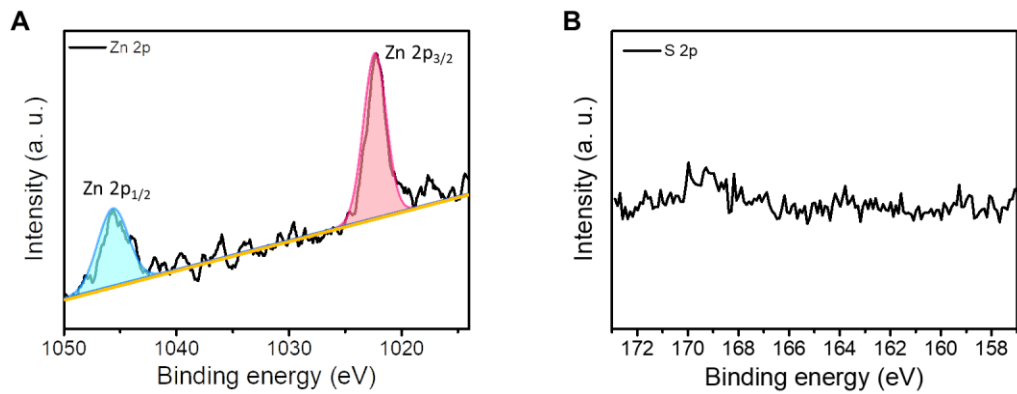
**Figure S9.** XPS results of SEBS-MA coated silicon wafer after being immersed in 2 M ZnSO$_4$ electrolyte.

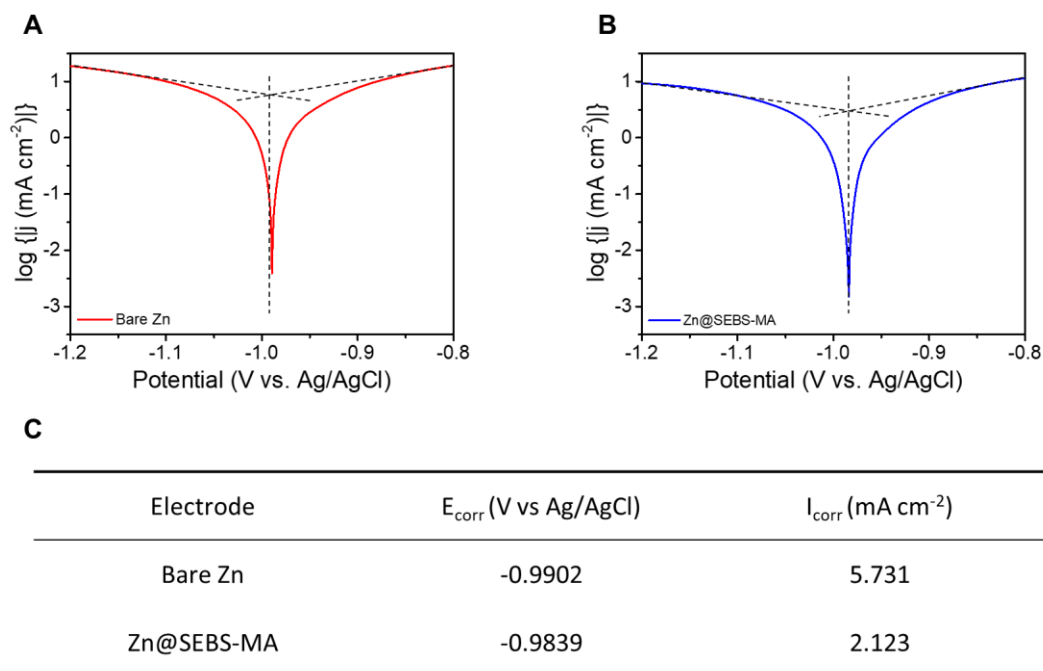XPS spectra of (A) Zn 2p and (B) S 2p.
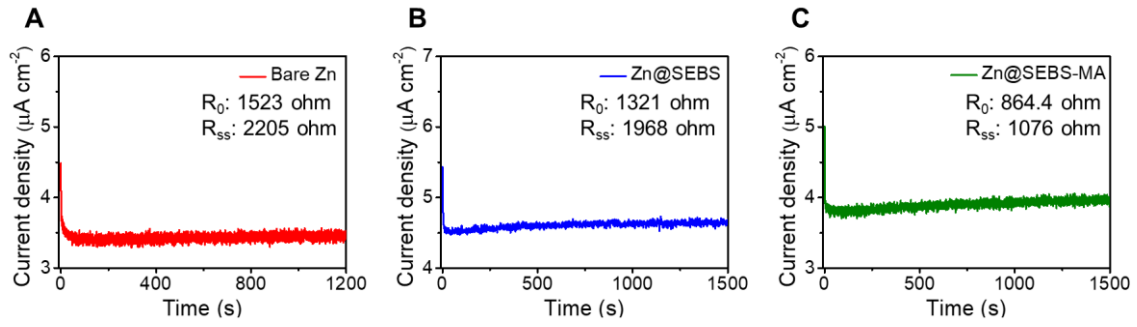
**Figure S10.** Transference number calculation of bare Zn, Zn@SEBS, and Zn@SEBS-MA electrodes.

(A-C) Current-time plots of bare Zn (A), Zn@SEBS (B), and Zn@SEBS-MA (C) symmetric cells with voltage polarization of 10 mV. The inset information exhibit EIS results of respective cells before ($R_0$) and after ($R_{ss}$) polarization applied.

The transference number of $Zn^{2+}$ ($t_{Zn^{2+}}$) was evaluated by the following equation:

$$t_{Zn^{2+}} = \frac{I_s(\Delta V - I_0 R_0)}{I_0(\Delta V - I_s R_s)}$$

where $\Delta V$ is the applied voltage polarization, $I_0$ and $R_0$ are the initial state current and resistance respectively, and $I_s$ and $R_s$ are the steady-state current and resistance respectively.

**A**

**B**

**C**

| Electrode | $E_{corr}$ (V vs Ag/AgCl) | $I_{corr}$ (mA cm$^{-2}$) |
|---|---|---|
| Bare Zn | -0.9902 | 5.731 |
| Zn@SEBS-MA | -0.9839 | 2.123 |

**Figure S11.** Investigation on the anti-corrosive behavior of SEBS-MA protective layer. (A-B) Linear polarization curves of bare Zn electrode (A), and Zn@SEBS-MA electrode (B). (C) Corrosion properties of bare Zn and SEBS-MA coated Zn electrode based on obtained linear polarization curves. $I_{corr}$ and $E_{corr}$ represent corrosion current density and corrosion potential respectively.
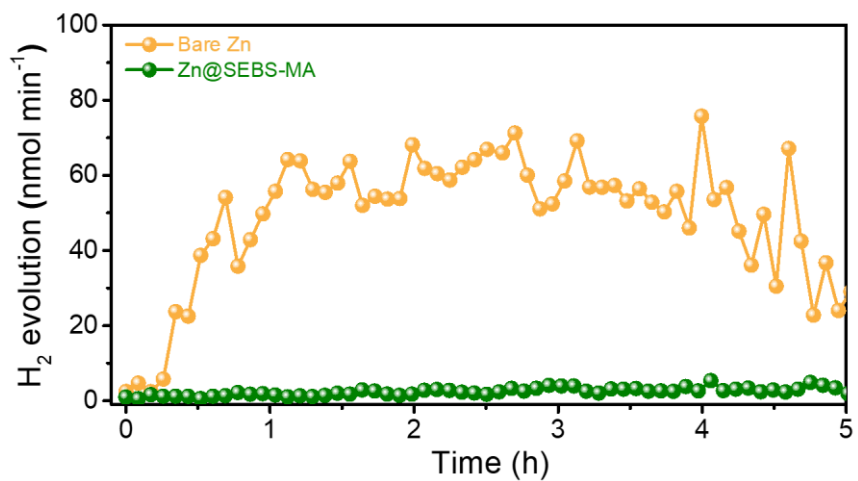
**Figure S12.** Differential electrochemical mass spectrometry analysis of the evolved $H_2$ gas with applying constant current (2 mA·cm$^{-2}$) for 5 h.
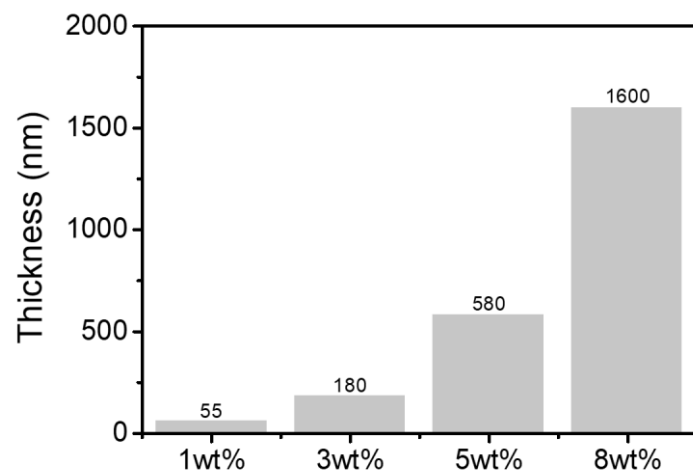
**Figure S13.** SEBS-MA coating layer thickness comparison by adjusting spin-coated polymer solution concentration (1wt%, 3wt%, 5wt% and 8wt%).
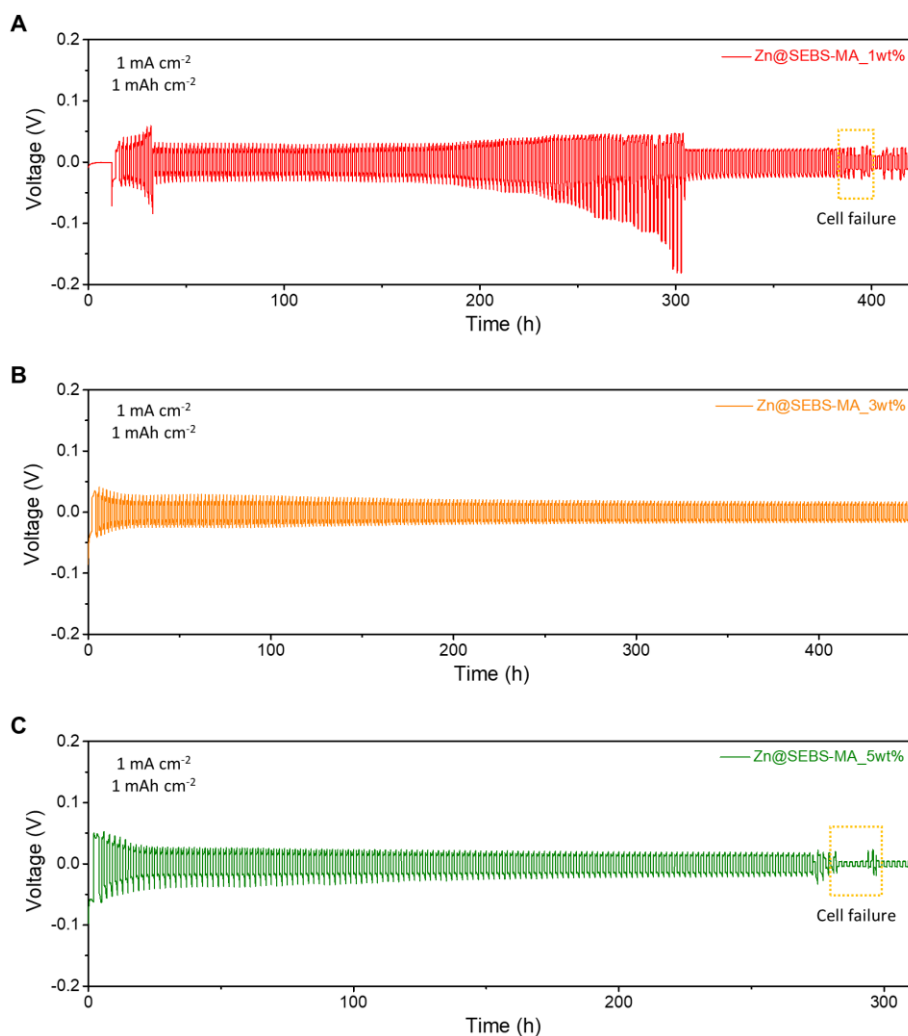
**Figure S14.** Symmetric cell performance based on Zn@SEBS-MA electrode with different coating layer thickness.

(A-C) Zn plating/stripping behaviors of Zn@SEBS-MA electrodes using 1wt% (A), 3wt% (B), and 5wt% (C) SEBS-MA dissolved in toluene solution during spin-coating process. The cell cycling was carried out at a current density of 1 mA cm$^{-2}$ and capacity of 1 mAh cm$^{-2}$. Note that Zn@SEBS-MA electrodes with different solution concentration showed inferior cycling behaviors and all electrochemical analysis in this paper were conducted using 3wt% SEBS-MA solution accordingly.
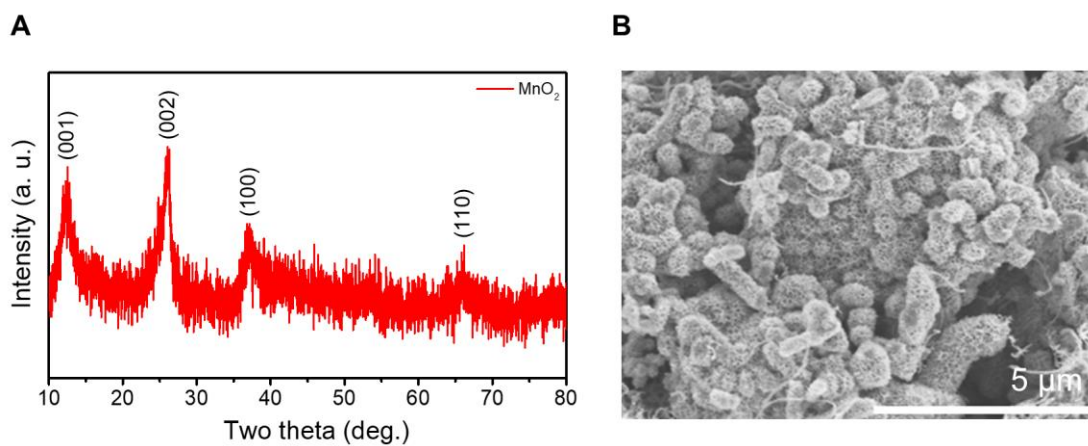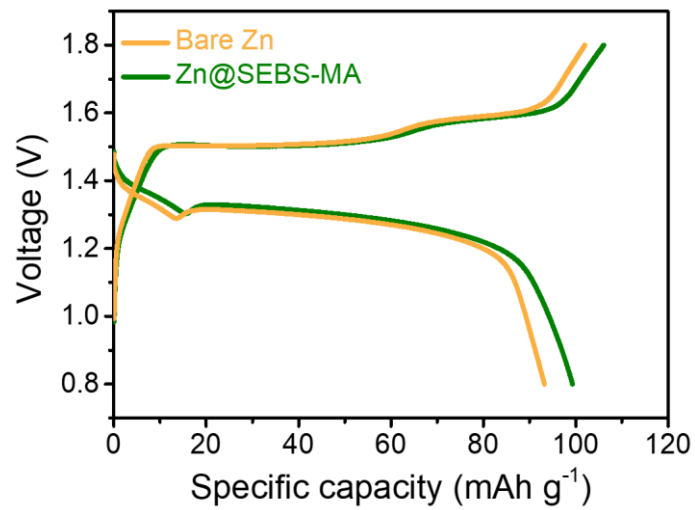
**Figure S15.** Characterization on carbon nanotube modified $MnO_2$ cathode material.

(A) XRD pattern of the synthesized carbon nanotube modified $MnO_2$ indicating well defined birnessite structure.[2]

(B) SEM image of the synthesized carbon nanotube modified $MnO_2$.

**Figure S16.** Charge-discharge profiles at the first cycle of Zn|$MnO_2$ and Zn@SEBS-MA|$MnO_2$ cells with a cycle rate of 0.5 C.

**Table S1**. The summary of various zinc ion batteries using surface-modified zinc anodes based on previously reported literatures.

| Electrode | Electrolyte | Areal Capacity (mAh·cm⁻²) | Applied Current density (mA·cm⁻²) | Life time (h) | Cumulative Capacity (mAh·cm⁻²) | Ref. |
|---|---|---|---|---|---|---|
| Zn@SEBS-MA | 2 M ZnSO$_4$ | 1 | 3 | 3160 | 4740 | This work |
| Zn@MXene | 2 M ZnSO$_4$ | 0.2 | 0.2 | 820 | 82 | 3 |
| Zn@NGO | 2 M ZnSO$_4$ | 5 | 5 | 300 | 750 | 4 |
| Zn@PA | 2 M ZnSO$_4$ | 0.25 | 0.5 | 8010 | 2002 | 5 |
| Zn@PVB | 1 M ZnSO$_4$ | 0.5 | 0.5 | 2200 | 550 | 6 |
| Zn@Kaolin | 2 M ZnSO$_4$ | 1.1 | 4.4 | 800 | 1760 | 7 |
| Zn@TiO$_2$ | 3 M Zn(SO$_3$CF$_3$)$_2$ | 1 | 1 | 150 | 75 | 8 |
| Zn@F-TiO$_2$ | 1 M ZnSO$_4$ | 2 | 2 | 280 | 280 | 9 |
| Zn@ZnO-3D | 2 M ZnSO$_4$ + 0.1 M MnSO$_4$ | 1.25 | 5 | 500 | 1250 | 10 |

**Supplemental References**

1.   Ghanta, S.R., Rao, M.H., and Muralidharan, K. (2013). Single-pot synthesis of zinc nanoparticles, borane ($BH_3$) and closo-dodecaborate ($B_{12}H_{12}$)$^{2-}$ using $LiBH_4$ under mild conditions. Dalt. Trans. 42, 8420–8425.

2.   Misnon, I.I., Aziz, R.A., Zain, N.K.M., Vidhyadharan, B., Krishnan, S.G., and Jose, R. (2014). High performance $MnO_2$ nanoflower electrode and the relationship between solvated ion size and specific capacitance in highly conductive electrolytes. Mater. Res. Bull. 57, 221–230.

3.   Zhang, N., Huang, S., Yuan, Z., Zhu, J., Zhao, Z., and Niu, Z. (2021). Direct Self-Assembly of MXene on Zn Anodes for Dendrite-Free Aqueous Zinc-Ion Batteries. Angew. Chem. Int. Ed. 60, 2861–2865.

4.   Zhou, J., Xie, M., Wu, F., Mei, Y., Hao, Y., Huang, R., Wei, G., Liu, A., Li, L., and Chen, R. (2021). Ultrathin Surface Coating of Nitrogen-Doped Graphene Enables Stable Zinc Anodes for Aqueous Zinc-Ion Batteries. Adv. Mater. 33, 2101649.

5.   Zhao, Z., Zhao, J., Hu, Z., Li, J., Li, J., Zhang, Y., Wang, C., and Cui, G. (2019). Long-life and deeply rechargeable aqueous Zn anodes enabled by a multifunctional brightener-inspired interphase. Energy Environ. Sci. 12, 1938–1949.

6.   Hao, J., Li, X., Zhang, S., Yang, F., Zeng, X., Zhang, S., Bo, G., Wang, C., and Guo, Z. (2020). Designing Dendrite-Free Zinc Anodes for Advanced Aqueous Zinc Batteries. Adv. Funct. Mater. 30, 2001263.

7.   Deng, C., Xie, X., Han, J., Tang, Y., Gao, J., Liu, C., Shi, X., Zhou, J., and Liang, S. (2020). A Sieve-Functional and Uniform-Porous Kaolin Layer toward Stable Zinc Metal Anode. Adv. Funct. Mater. 30, 2000599.

8.   Zhao, K., Wang, C., Yu, Y., Yan, M., Wei, Q., He, P., Dong, Y., Zhang, Z., Wang, X., and Mai, L. (2018). Ultrathin Surface Coating Enables Stabilized Zinc Metal Anode. Adv. Mater. Interfaces 5, 1800848.

9.   Zhang, Q., Luan, J., Huang, X., Wang, Q., Sun, D., Tang, Y., Ji, X., and Wang, H. (2020). Revealing the role of crystal orientation of protective layers for stable zinc anode. Nat. Commun. 11, 3961.

10.  Xie, X., Liang, S., Gao, J., Guo, S., Guo, J., Wang, C., Xu, G., Wu, X., Chen, G., and Zhou, J. (2020). Manipulating the ion-transfer kinetics and interface stability for high-performance zinc metal anodes. Energy Environ. Sci. 13, 503–510.